INVESTIGATION OF NON-PLATINUM GROUP METAL CATALYSTS FOR PURE WATER ANION EXCHANGE MEMBRANE ELECTROLYSIS

by

SARAH BEAUDOIN

A THESIS

Presented to the Department of Chemistry and Biochemistry
and the Robert D. Clark Honors College
in partial fulfillment of the requirements for the degree of
Bachelor of Science

May 2023

An Abstract of the Thesis of

Sarah Beaudoin for the degree of Bachelor of Science
in the Department of Chemistry and Biochemistry to be taken June 2023

Title: Investigation of Non-Platinum Group Metal Catalysts for Pure-Water Anion Exchange Membrane Electrolysis

Approved: *Shannon Boettcher, Ph.D.*
Primary Thesis Advisor

Pure water anion exchange membrane water electrolyzers (AEMWEs) show promise for utilizing renewable energy and non-platinum group metal (non-PGM) catalysts to create clean hydrogen fuel. Being a new technology, AEMWEs lack standardized procedures and materials, limiting reproductivity and expansion. Furthermore, complex interactions between the ionomer and catalyst during the oxygen evolution are not well understood, resulting in a lack of baseline performance and therefore scalability. In the following study, five anodic non-PGM catalysts, alongside current baseline catalyst IrO_2, are analyzed for their activity, durability, and restructuring in AEMWE. We found that electronic conductivity plays the most significant role in determining metal oxide catalyst performance in AEMWEs, scaling linearly with increasing electrical conductivity. Co_3O_4 was found to exhibit high performance and electronic conductivity in AEMWEs, therefore five cobalt oxides were chosen to be further studied in AEMWE systems, focusing on the role of conductivity, OER performance, and durability. The results reveal that conductivity is critical in determining the activity of a catalyst in AEMWE, but that practical ionomer loading causes electronically insulative effects. Further, it was found that catalyst restructuring during operation results in negative ionomer interactions, hindering OER activity and long-term stability.

Acknowledgements

I would like to express my sincerest thanks to Professor Shannon Boettcher, Professor Samantha Hopkins, and Dr. Grace Lindquist for acting as my thesis committee. Grace Lindquist, in particular, has provided incredible guidance, inspiration, and instruction as I carried out research and wrote my thesis and has been contributed in infinite ways to my academic career. This research would also not have been possible without the ingenuity, encouragement, and previous works of Professor Shannon Boettcher. I would also like to thank Ms. Miriam Jordan of the Clark Honors College for providing this excellent template and ensuring that this thesis meets all formatting criteria. I am thankful for the entire Boettcher lab group for their continued patience, kindness, and contributions to this research project, specifically Ally Tonsberg, for her friendship over the last three years. Finally, I would like to thank my family for their patience and support throughout my academic career. Funding for this work came from the Vice President of Research and Innovation and the University of Oregon Summer Program for Undergraduate Research and the Stamps Family Charitable Foundation. This would not have been possible without all of you.

Table of Contents

List of Figures

Introduction

Hydrogen As Fuel

It is well known that the excessive and persistent use of fossil fuels around the world has led us to the brink of a climate crisis. Renewable energy from sources such as solar, wind, and hydroelectric power are promising alternatives for energy production, but must be expanded and refined to meet current energy demands. Renewable energy sources lack consistency and the capacity for storage, necessary features for reliable large-scale industrial, commercial, and residential grid implementation. The clean creation of hydrogen gas (H_2) through water electrolysis has been proposed as an energy-storage solution to stabilize the fluctuating load of renewable energy currently available.[1]

Hydrogen gas (H_2) currently has a wide range of important applications including fertilizer production, powering vehicles and buildings, heating, refining metals, and, more recently, storing energy from renewable resource grids. As the world turns away from the burning of fossil fuels, H_2 will become an increasingly crucial component of our global energy market. Figure 1, from the US Department of Energy's H2@Scale initiative, depicts a multi-faceted approach to the creation and widespread implementation of hydrogen fuel.[2] Such an interconnected system can only be implemented if clean hydrogen fuel generation can become economically and energetically competitive with the current fossil fuel market. Globally, as of 2021, more than 95% of hydrogen production was still derived from the combustion of fossil fuels.[3] A substantial scale-up of electrolysis technology is necessary to meet current H_2 demands.

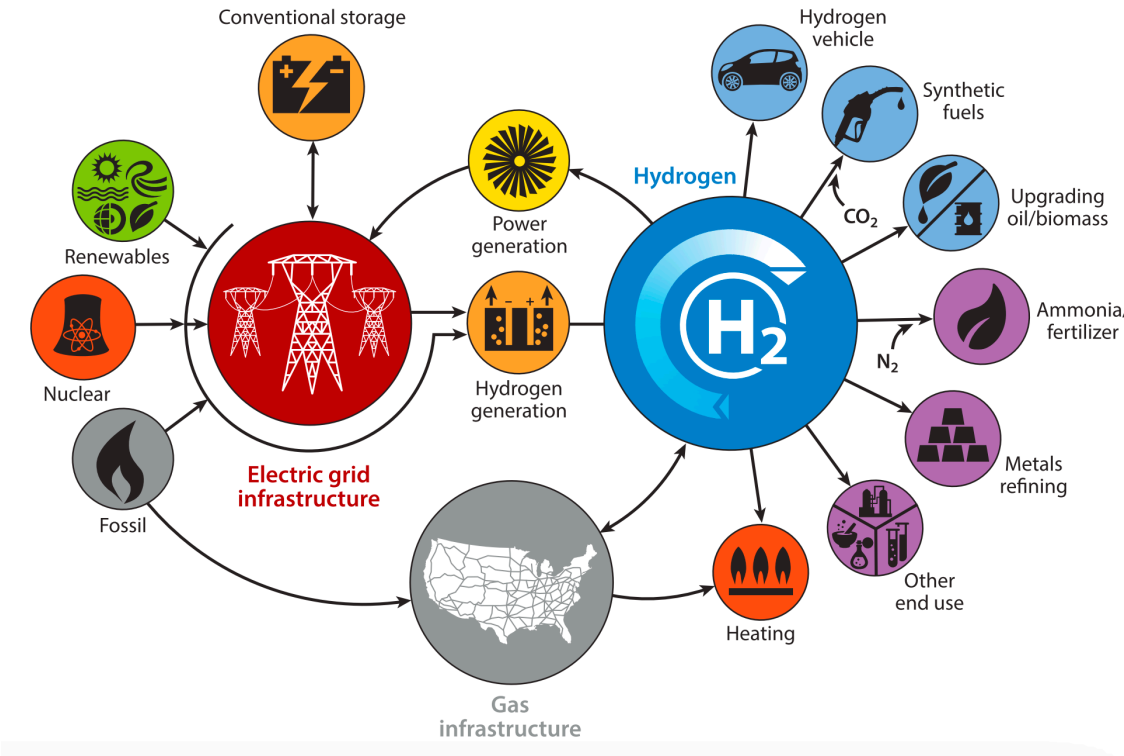

Figure 1. Proposed Hydrogen Fuel Economy from the U.S. Department of Energy

Adapted from Ref[2].

Electrolyzer Technology

While much of the hydrogen produced today requires the burning of fossil fuels and is therefore increasing the amount of greenhouse gases in our atmosphere, developing technologies have the potential to create carbon neutral H_2 via water electrolysis.[1] Water electrolysis is a process that splits liquid H_2O into its independent constituents, forming H_2 and O_2 gas. Alkaline water electrolysis (AWE) is the most mature and largest scale electrolyzer technology, and has been used for hydrogen production since the 1800s with great reliability and low cost.[1] AWE allows for the use of relatively cheap materials, such as stainless steel and non-PGM catalysts.[4] However, these systems operate at low (atmospheric) pressure and low current density, resulting in less efficient hydrogen production, as well as require large quantities of concentrated electrolyte.[1,5]

Membrane electrolyzers are preferred for industry-scale H_2 production, for their high-purity hydrogen production, lack of corrosive electrolytes, and ability to generate ready-to-use, pressurized hydrogen.[6] Membrane electrolyzers use a solid polymer membrane to facilitate the separation of oppositely charged ions, allowing hydrogen and oxygen gas to form at each electrode on opposite sides of the membrane. Throughout the previous decade, proton-exchange membrane (PEM) electrolyzers have been the focus of much water-splitting technology research due to their very pure hydrogen production, lack of corrosive electrolytes, ability to generate ready-to-use, pressurized hydrogen, and their relative simplicity of operation, requiring only deionized water and an energy source.[6] However, the locally acidic conditions created by the proton-selective membrane necessitate the use of expensive materials that resist corrosion, such as platinum-group-metal (PGM) catalysts and titanium hardware.[4]

A third type of electrolyzer, utilizing an anion exchange membrane (AEM), has recently shown promise for integrating the benefits of the AWE and PEM systems into one technology. AEM utilizes a polymer membrane with fixed internal positive charges, acting as a liquid electrolyte to drive negative anions through the system. Similar to PEM water electrolyzers, AEM water electrolyzers (AEMWE) require only pure water and energy to operate, and produce pressurized, pure hydrogen gas. Unlike PEM systems, AEM create a locally alkaline environment due to the movement of hydroxides through the positively changed membrane. Therefore, the benefits of AWE systems, such as low-cost materials and non-PGM catalysts, are also available for AEM electrolyzers.[5] Although AEMWE have significant benefits over previous technologies, lack of stability and durability of the membranes themselves has limited growth and this discrepancy must be solved before AEMWE can reach their full potential. See Figure 2 for an illustration of the three main electrolyzer types.

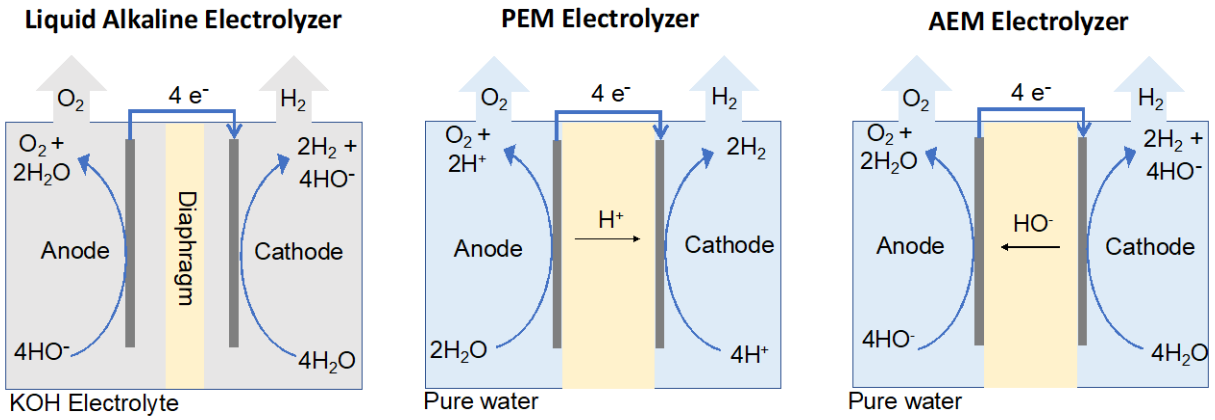

Figure 2. Generalized schematic of the three major types of electrolyzers

Liquid Alkaline, Proton Exchange Membrane (PEM), and Anion Exchange Membrane (AEM).[1]

The following study will focus on expanding the knowledge and applications of anion exchange membrane technology through the study of non-PGM catalysts. By testing various catalysts for use in an anion exchange membrane electrolyzer, isolation of a stable and active catalyst for AEMWEs may be possible, improving accessibility and lowering the cost of carbon-neutral hydrogen fuel production. Furthermore, we hope to gain an enhanced understanding of how various metal-oxides affect degradation of the anion-conducting polymer. Altogether, this comprehensive study will contribute to our understanding of the fundamental features of performance and durability in AEMWE, therefore assisting in their eventual utilization in a green hydrogen economy.

Scientific Background

Oxygen Evolution

Theoretically, the formation of $O_2(g)$ and H2(g) from $H_2O(l)$ by the oxygen evolution reaction should require 1.23 V of applied potential.[7] The necessary half-reactions are provided

below as the hydrogen evolution reaction (HER), shown in Equation 1, and the oxygen evolution reaction (OER), shown in Equation 2.

(1) HER: $4e^- + 4H_2O(l) \rightarrow 2H_2(g) + OH^-(aq)$

(2) OER: $4OH^-(aq) \rightarrow O_2(g) + 2H_2O(l) + 4e^-$

Resistivities from physical factors like the travel path of electrons through the wires, cathode, and anode, as well as any energy lost to conductivity differences between membrane surfaces within the cell causes the actual energy required for this process to be greater. Of the two reactions, the oxygen evolution reaction requires a greater overpotential of energy due to its kinetically strenuous 4-electron oxidation process. Such overpotential significantly reduces the efficiency of the process and the feasibility of using electrolysis as an accessible source of energy storage.

To mitigate this overpotential, various metal catalysts have been developed for both the surface of the anode and cathode, which reduce overpotential and increase the efficiency of electrolyzer technology. Current conventional catalysts for the OER are made from costly and rare platinum-group metals, most commonly iridium oxides (IrO_2).[6] These metals are active and durable within the harsh acidic conditions of the PEM cell. However, the high cost and limited supply chain for these metals limits expansion into commercial and private fields. Developments in the branch of electrolysis dealing with using anion exchange membranes (AEM), as opposed to PEM, allow for the use of non-platinum-group-metal (non-PGM) catalysts in place of platinum-group metals.[8] Nickel (Ni), iron (Fe), cobalt (Co) oxide-based catalysts have shown the highest activity for OER in alkaline systems and are therefore of substantial research interest for AEM electrolyzers.[9,10]

Anion Exchange Membrane Water Electrolyzers

Anion Exchange Membrane Water Electrolysis (AEMWE) uses an anion-selective membrane sandwiched between two electrodes. The structure of the commercially available membrane used for this study, PiperION TP-85, is shown in Figure 3. When current is applied, H_2O is reduced to hydroxide ions (OH^-) and H_2. OH^- is driven across the AEM to the anode, where it is oxidized to form O_2 and H_2O are formed (see Figure 4a[11]).

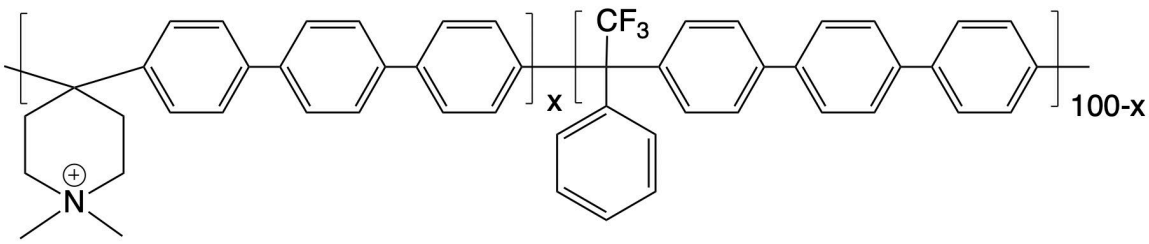

Figure 3. Chemical Structure of PiperION TP-85 by Versogen

Adapted from Ref[12].

In industrially-relevant AEM systems, the membrane is compressed between the anode and cathode plates, which consist of a thin layer of catalyst applied to the surface of an appropriate porous substrate, known as a gas diffusion layer (GDL). The GDL must be porous enough for the transport of ions and water, but electronically conductive and fine enough to support the applied catalyst in the form of a liquid ink. Typically, the GDL is a fine stainless steel mesh at the anode and carbon paper at the cathode. A cross section of the AEM material sandwhich can be seen in Figure 4a.

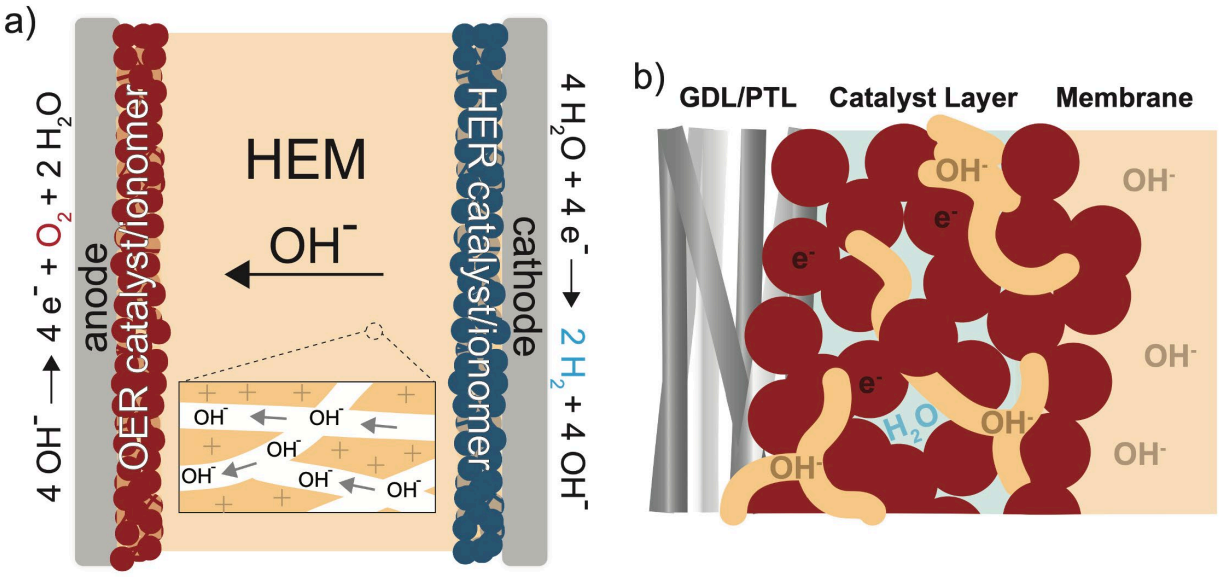

Figure 4. Schematic of Anion Exchange Membrane Electrolyzer

a) Cross section of AEM electrolyzer b) Close up illustration of anodic catalyst and ionomer interface

To mitigate junction resistivities at the boundary between the catalyst and the membrane and facilitate the movement of ions through the catalyst layer to the GDL a small amount of diluted, solvated, membrane is introduced into the catalyst layer itself, known as ionomer. This is done by adding ionomer to the catalyst ink and incorporating thoroughly before application to the GDL. All catalyst inks studied in this paper contain ionomer, unless overwise noted. Ionomer is also applied to the surface of the catalyst layer where it meets the membrane, displayed illustratively in Figure 4b. While the charged membrane and ionomer is a necessary component of the AEM, it is also susceptible to degradation via nucleophilic attack by OH^-, oxidation at the junction of the catalyst surface, and oxidation by OER intermediate species and oxygen radicals.[13,14] The interactions between the catalyst, ionomer, membrane, and GDL during OER are complex and must be considered when analyzing results from an AEMWE.[14]

Chapter One: Ionomer-Catalyst Interactions (2020-2021)

Literature Review

The most significant obstacle to implementing AEM electrolysis commercially is membrane performance.[1] Membranes must be ionically conductive to efficiently transport hydroxide ions from the cathode to the anode, and need to remain stable during extended use, avoiding oxidation and other degradation pathways. Increasing membrane ionic conductivity typically leads to a decrease in stability due to an increased water uptake and solubility.[15,16] In order to stay commercially relevant and compete with PEM systems that can operate for days before serious degradation occurs, most AEM membranes sacrifice ionic conductivity for increased durability.[15,17,18] In order to compensate for lower ionic conductivity, many AEM electrolyzers utilize dilute alkaline electrolytes, which increase the availability of OH^- for the OER. Under this regime high AEM performance has been achieved,[19] however removing supporting electrolytes and operating with only deionized (DI) water will be necessary for large-scale implementation of AEM electrolysis to simplify maintenance and complete with available pure-water PEM systems.[6]

Pure-water AEM electrolysis shows promise in achieving low-voltage potentials at 1 A cm^{-2}, but a lack of standardization within the field causes a lack of reproducibility and baseline performance. Limited or over-specified protocol standardization is a significant issue when attempting to reproduce results and can cause discrepancies in operated performance. For instance, various storage routines, ion exchange procedures, deposition methods, catalyst integration, and deposition techniques of the ionomer can all exhibit different behavior during operation.[20] As performance losses due to ionomer degradation are difficult to deconvolute from inherent catalyst performance, reducing variables is crucial in revealing the true performance of catalysts.

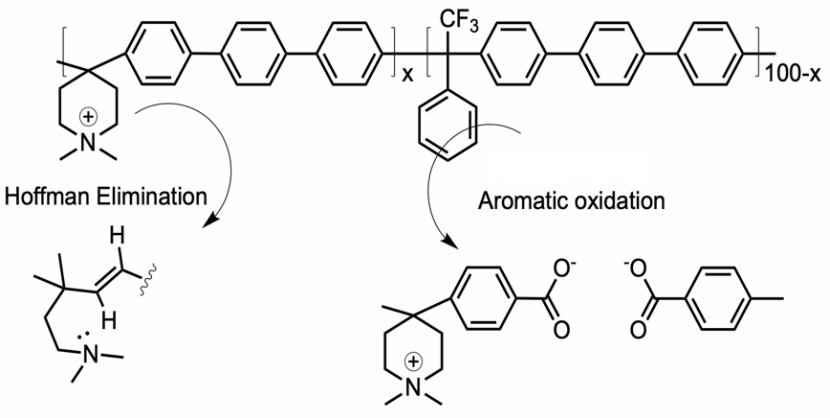

Figure 5. Two possible mechanisms of ionomer degradation in AEM.

Adapted with permission from Ref[15].

Detachment of the ionomer binder from the catalyst surface, chemical ionomer poisoning, poor ionomer distribution, connectivity issues between the catalyst layer and membrane, and catalyst dissolution and redeposition are all factors that could contribute to increased cell voltage.[12,15,21,22] Chemical degradation pathways of the ionomer of interest PiperION TP-85, are described in Figure 5. Shown in Figure 4b, the junction between the catalyst and ionomer may be the most likely location for ionomer oxidation due to the high volume of oxidizing reactions occurring on the anode.[15] These performance loss pathways are further complicated in the presence of non-PGM catalysts, which sometimes exhibit dissolution and restructuring to a greater extent than oxidatively stable IrO_2.[8,23]

Findings

Nuclear magnetic resonance (NMR) testing was conducted on our membrane material at various stages of catalyst testing to compare with the literature value for PiperION TP-85 (Fig. 6) and ensure no degradation had occurred as a result of procedural techniques. Hydrogen NMR is a technique which provides information about specifically the hydrogens in a (typically organic) molecule sample, such as what their chemical environment was at the time of testing. Different

chemical environments will result in the hydrogen having a higher or lower chemical shift (ppm), that is being shielded or de-shielded from the instruments magnetic field by the surrounding atoms. Because the ionomer chain used to conduct anions is an organic molecule, we were able to study its quality and determine if our procedure for handling the membrane was optimized.

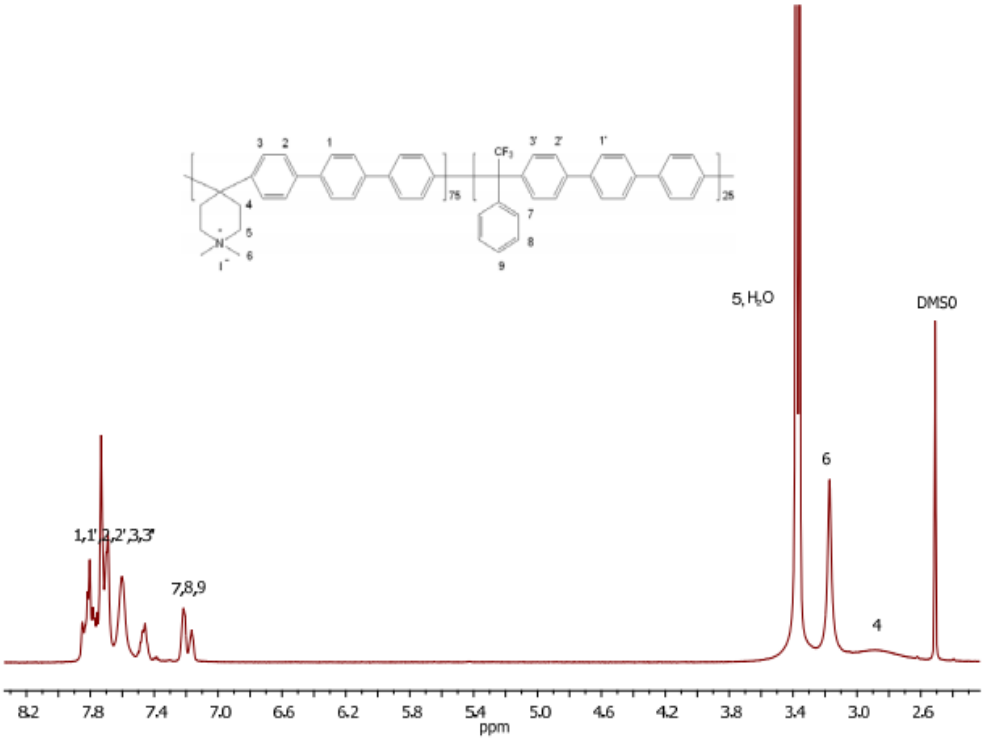

Figure 6. Literature sourced NMR spectrum of PiperION TP-85 polymer with peaks labelled. Adapted with permission from Ref[13].

The first discovery made using NMR analysis was the appearance of multiple new peaks in the spectra of ionomer taken from a pristine, spray coated electrode. This spectrum is shown in red in Figure 7. Due to their chemical shift being between 7.0 and 4.5 ppm, along with collaboration with our industrial partners who supplied the polymer products, we determined that these peaks were likely products from the Hoffman Elimination (Figure 5). The Hoffman Elimination would occur if charged hydroxide ions (either from use or from membrane conditioning in KOH) were allowed to remain in the ionomer structure, attached to the positively charged nitrogen groups, while the

membrane was dries. If the membrane is hydrated, each hydroxide will attract a solvation shell of polar water molecules which diffuse its charge and therefore its ability undergo to nucleophilic attack of the nitrogen. Hoffman Elimination alters the structure of the polymer by neutralizing essential charge groups that pull anions through the membrane, therefore greatly decreasing its ability to conduct ions. As the ionomer experiences multiple wet- and dry-stages throughout its production and use, this mechanism could have a significant impact on the efficiency of the system.

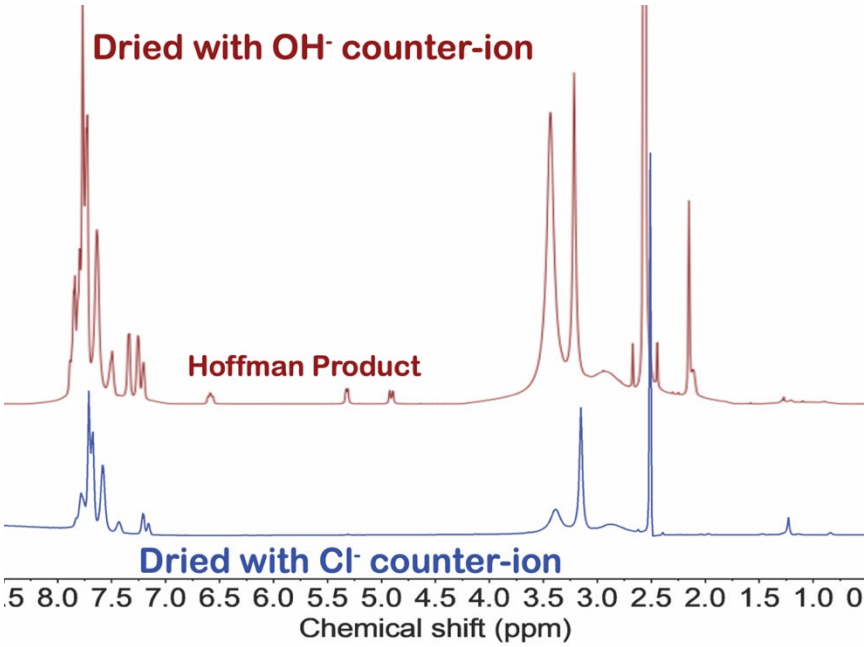

Figure 7. NMR Spectra before and after the use of quenching to eliminate the Hoffman product. Collected 2021.

One solution to this method of degradation is to replace the hydroxide with chloride (Cl^-). Because Cl^- has a greater electron affinity than oxygen, it will be less likely to exhibit nucleophilic attack. Ion exchange within the membrane and electrodes can be done via a process called quenching, in which the sample is allowed to rest in a solution of hydrochloric acid (HCl, 1M) or sodium chloride (NaCl, 3 M) for at least 1 hour before being rinsed with 18.2 MΩ cm water and then dried. By introducing this quenching step before completing NMR testing, we found that the Hoffman Elimination product peaks were completely avoided, as shown by the blue spectra in Figure 7.

The practice of quenching AEM membranes with this technique is now common within our lab and included in a standard operating procedure for post-operation membrane electrode assembly analysis.[24]

Chapter Three: Exploration of Non-Platinum Group Metals (2020-2021)

Literature Review

Non-Platinum-Group-Metal Catalysts

In an effort to uncover the convoluted relationship between OER activity in AEM and liquid electrolyte systems, we needed to explore numerous characteristics of the catalyst oxides, the ionomer material, and how they interact during cell use. Commercially available iridium oxide (IrO_2) has shown high activity and long-term stability but is cost prohibitive for large-scale applications.[15] Non-PGM catalysts are cost effective, but underdeveloped, therefore little is known about their potential when used in a pure water-fed electrolyzer. However, existing information on non-PGM oxides such as cobalt (Co), nickel (Ni), iron (Fe) tested within 3-electrode half-cells[9,10] in combination with commercial availability allowed us to choose five non-PGM catalysts for this portion of the study: NiO, $NiFe_2O_4$, Co_3O_4, $NiCoO_2$, and $NiCoFe_2O_4$. Catalyst performance was compared to IrO_2 as a baseline OER catalyst for AEM systems.[15,22,18]The latter half of this chapter is devoted to the study of these catalysts and their interaction with the membrane, which will also affect their potential uses and scalability.

Oxyhydroxides

Metal oxide catalysts, like the ones discussed in this paper, each have a unique characteristic crystal structure and properties that affect their performance as OER catalysts. It has been discovered that, upon applying oxidizing potential, their surfaces will restructure to various degrees into amorphous or layered oxyhydroxide species.[25–30] These evolutions occur as a function of parameters like method of deposition, mass loading, electrolyte, size of particle, initial oxidation state, and elemental composition.

Oxyhydroxides of metals, generically $MO_x(OH)_y$ or MO_xH_y, have gained interest in the field of electrolysis since the discovery of the highly active $Ni_{0.9}Fe_{0.1}OOH$ species having an OER turnover frequency more than 10 times greater than that of the current industry standard, IrO_2, in alkaline electrolyte.[30,31] Fe is a crucial component in the OER in alkaline media, increasing the activity of Co and Ni based oxide catalysts significantly.[4,32] However, Fe on its own is a poor electrical conductor and is susceptible to leaching and lack of stability. For this reason, recent work on non-PGM catalysts for OER in base have focused mixed-metal oxides consisting of on Fe paired with Ni, Co, or both. Ni and Co have higher intrinsic conductivity and stability than Fe, exhibiting a lower propensity for dissolution and redeposition under applied potential, but also have lower OER activity compared to Fe, with Co exhibiting the worst OER performance in alkaline media.[22,25]

The potential properties of Fe-Ni-Co oxyhydroxide catalysts in AEM systems have remained convoluted over the last decade, especially in AEM systems. $NiFeO_xH_y$, a high performing catalyst in alkaline conditions, displays the worst performance in pure water AEMs using a solid anion conducting membrane.[22] This can be explained by the low electrical conductivity of Fe-based oxides before being exposed to an oxidizing current. In a pure water environment, as opposed to alkaline electrolyte, the necessary oxidation only occurs at the boundary with the anion-conducting ionomer, therefore the bulk material of the catalyst remains electronically insulative, causing poor OER activity.[22] The following study will contribute to current knowledge in the field by considering the potential catalyst evolution to oxyhydroxide forms in both alkaline electrolyte and pure water.

Results and Discussion

The following chapter details an extensive investigation of earth-abundant anode catalysts for pure water AEMWE. It was our goal to test the activity and stability of various non-PGM catalysts for the oxygen evolution reaction (OER) in an AEM cell to reduce cost and increase scalability of electrolyzer technology. In theory, these catalysts could improve accessibility and lower costs for hydrogen producing electrolyzers, therefore assisting in the production of clean-burning fuel and mitigating the need for fossils fuels. Furthering our understanding of this topic will aid in the fundamental understanding of metal-oxide performance and durability in AEMWEs, and the relationship between non-PGM conductivity and performance in AEM electrolyzers.

Anode electrodes were prepared (see Experimental) using NiO, $NiFe_2O_4$, IrO_2, Co_3O_4, $NiCoO_2$, and $NiCoFe_2O_4$. These catalysts were all chosen due to their industrial availability, potential for competitive performance in alkaline media, and unexplained behavior within AEM electrolyzers.[8,15] For consistency Pt Black nanoparticles were used as the cathode catalyst in relevant systems and the same ionomer, PiperION TP-85 is used for all testing. Although it is a platinum-group-metal, IrO_2 was used as a baseline for comparison during catalyst activity and durability testing because it is the current industry standard.[10]

Assessment of each catalyst utilized pure water electrolyzer testing for in-situ activity and durability and alkaline electrolyte three-electrode half-cell testing using a quartz-crystal microbalance working electrode. Relevant X-ray photoelectron spectroscopy (XPS) for ex-situ composition analysis is included. Due to the apparent instability of AEM membranes, degradation and resistance of the membrane polymer was also studied in detail to deconvolute a multi-faceted loss of function during and outside of use. This was done via nuclear magnetic resonance (NMR) analysis and electrolyzer testing.

Non-PGM Activity and Durability

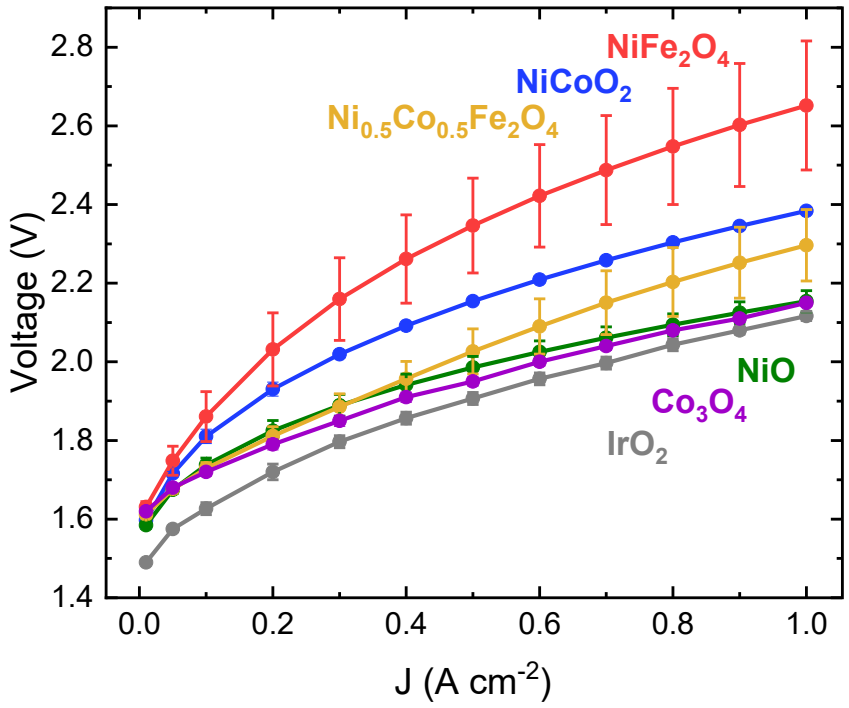

Figure 8. Stepped Chronopotentiometry polarization curve in AEMWE at 57 °C.

Sample size n=3; data presented is the average and error is one standard deviation. Collected 2021.

The first measurement for each catalyst was assessing the performance and durability of each in a pure-water anion exchange membrane electrolyzer. Figure 8 shows the measured cell voltage response to an applied current. Low applied current corresponds most to the inherent catalyst activity for OER, as ohmic losses due to high current movement and mass transport of gasses through the electrolyzer are negligible here. As current increases, ohmic losses begin to contribute, showing a linear voltage response. The upper range of current most accurately reflects the actual activity of the catalyst under ideal operating conditions, wherein current is high enough to produce gases at an economic rate. High current activity, which is not tested here, would be dictated by the resistance of the materials within the cell and the movement of ions and gases

through the system. IrO_2 shows the greatest activity throughout the entire test, followed closely by Co_3O_4. At low current $NiFe_2O_4$ is the least active and shows increasing loss of activity at higher applied current, likely due to its highly resistive nature. Similar, but less drastic, results are seen from $NiCoFe_2O_4$. As current increases, the initial disparity between IrO_2 and Co_3O_4 is reduced to only 50 mV, with NiO following closely behind Co_3O_4 in activity.

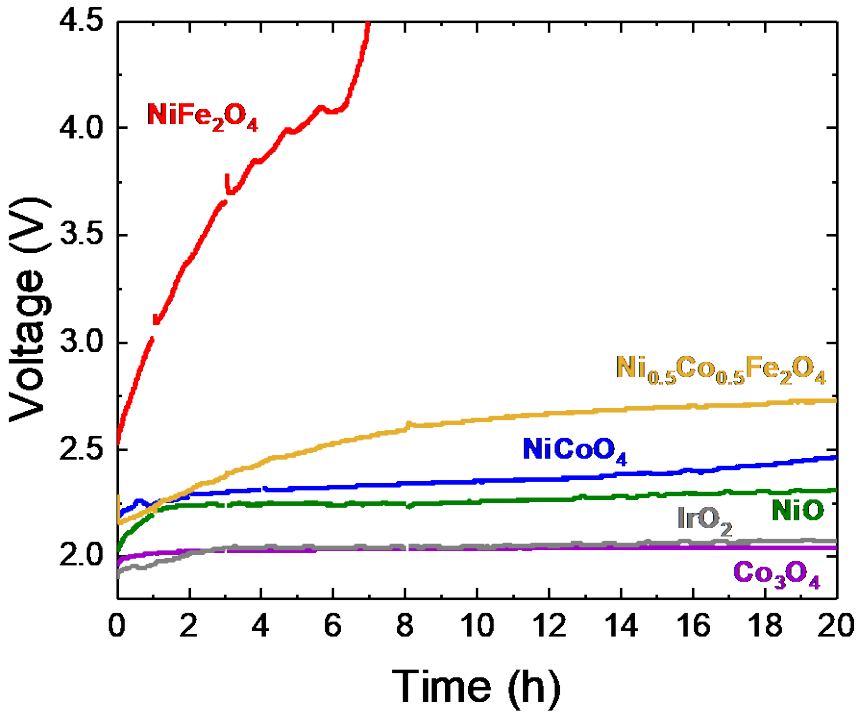

Figure 9. Extended Chronopotentiometry at 500 mA for 20 hrs in AEMWE at 57 °C.

Sample size n=1; data presented as one extended measurement for each catalyst. Collected 2021.

Next, the durability of each system was tested by monitoring cell voltage over time at a constant potential of 500 mA cm^{-2}, displayed in Figure 9 (vertical interruptions were caused by intermediate impedance testing and can be disregarded). $NiFe_2O_4$ rapidly increases in voltage to impractical levels (> 5 V) at around ~4 hours of testing. $NiCoFe_2O_4$ remains relatively stable, but at high operating voltage. IrO_2 and Co_3O_4 show highly stable behavior for most of the test,

degrading to ~2.1 V after 20 h of operation. Although NiO performed well in the activity tests, it exhibited greater initial degradation over the first hour of extended applied current, resulting in a higher, but stable, degradation profile ending at ~2.3 V after 20 h.

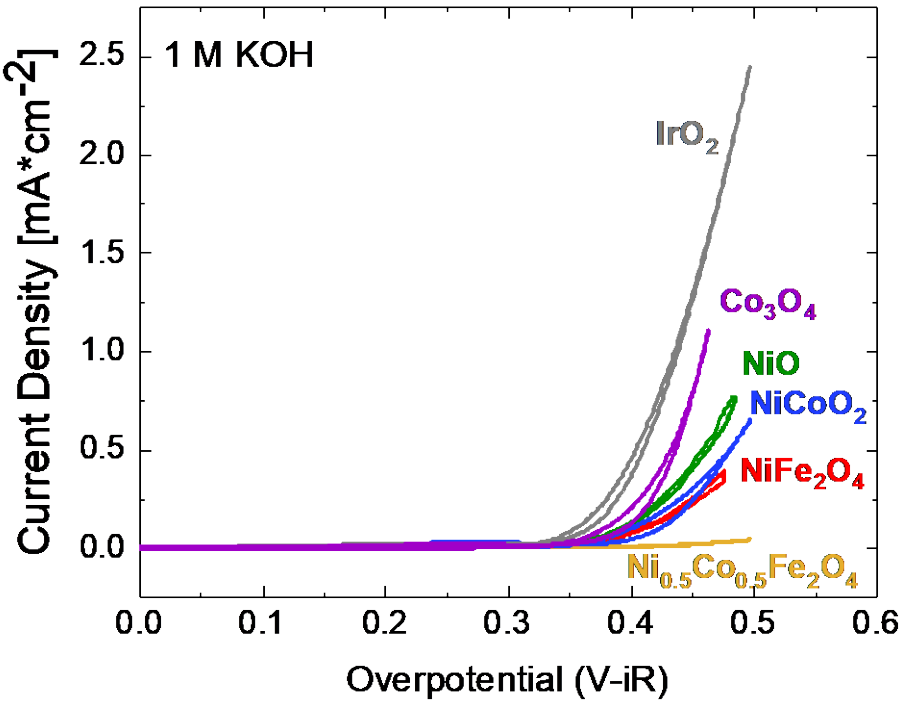

Figure 10. Cyclic voltammetry in three-electrode half-cell with 1M KOH electrolyte. Sample size n=3; data presented as average of three first cycles for each catalyst. Voltage has been corrected to overpotential by subtracting system resistivities (iR). Collected 2021 by Raina Krivina and Nathan Stovall.[23]

The same catalysts inks were tested in a three-electrode half-cell on a quartz-crystal microbalance to assess the activity of the catalysts more easily without potential interference from membrane degradation and to determine catalyst performance in liquid electrolyte conditions. In alkaline electrolyte, the transport of hydroxide to the active sites is more efficient, therefore the activity is more reliant upon catalyst activity, and not ionomer interactions. Figure 10 depicts the measured current density during a sweep of applied voltage from 0.0 to 0.9 V; data shown is from

average of three first cycles for each catalyst. The results from KOH three-electrode experiments agree with findings from the MEA, that is, IrO_2 outperforms all non-PGM catalysts, but is followed in activity by Co_3O_4.

These experiments aimed to reveal trends in non-PGM catalyst activity and durability in in-situ conditions as well as the relationship between these key catalytic features. Results from Figures 8, 9, and 10 reveal that Co_3O_4 is the highest preforming non-PGM in both half-cell and electrolyzer conditions, showing comparable performance and durability to IrO_2 in all trials. Interestingly, single metal oxides, such as Co_3O_4 and NiO, perform best and mixed-metal oxides, such as $NiFe_2O_4$, $Ni_{0.5}Co_{0.5}Fe_2O_4$, and $NiCo_2O_4$ exhibit unstable performance, increased degradation, and lower activity. The Fe-containing catalysts $NiFe_2O_4$ and $Ni_{0.5}Co_{0.5}Fe_2O_4$ perform poorly in all tests, despite previous studies indicating that the presence of Fe greatly increases the activity of both Co- and Ni-based OER catalysts in alkaline electrolyte.[27,31]This is likely due to the deposition method and catalyst structure, which results in greater amounts of "bulk" catalyst that cannot be accessed due to low electronic conductivity of the catalyst and reduces the ability of the metals to form the highly active oxyhydroxide state.[23,32]

Non-PGM Conductivity

Catalyst conductivity was measured to compare to activity data. Catalyst powders were pressed between two stainless steel discs at 23,000 psi. A voltage was swept from -1 V to 1V and the resulting current response was measured. The slope of the applied voltage over measured current yields the catalyst resistance. Then, conductivity was determined using the following equitation, $\sigma = {}^{l}/_{R * A}$, where l is the length of the catalyst layer, R is the resistance (${}^{V}/_{I}$), and A is the area of the catalyst disc. The data from these tests is shown in Figure 11.

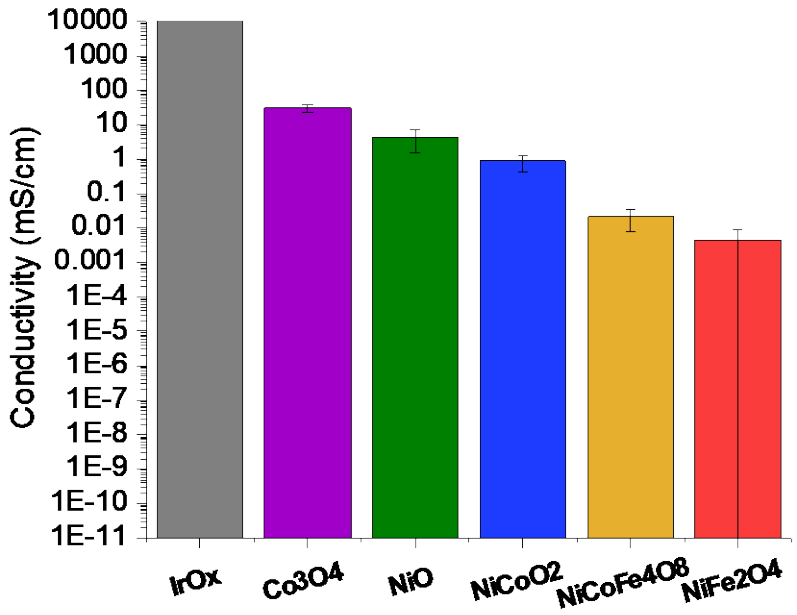

Figure 11. Processed data from chronoamperometry of catalyst powder in pellet press at 23,000 psi.

Sample size n=3; data presented with mean as bars and standard deviation as error. Collected 2022 by Grace Lindquist.[23]

Catalyst activity traits are directly proportional to conductivity, with IrO_2 having resistance comparable to that of the blank stainless-steel discs. The follow up, Co_3O_4, has the highest conductivity of the non-PGMs and the best performance of the non-PGMs in all testing. Increased conductivity of a catalyst indicates that more active sites are available for OER to occur, as electron transport through the material is less hindered and bulk interior catalyst is more accessible. Contrarily, the mixed-metal catalysts show very low conductivity, likely resulting in greater bulk interior catalyst which is unable to form active oxyhydroxide structure nor participate in OER.

From the data presented, catalyst electronic conductivity and performance in pure water AEM electrolyzers are directly proportional, with IrO_2 and Co_3O_4 having the highest conductivity and reliably high activity over extended testing conditions. Ni- and Fe-based catalysts exhibit

lower conductivity, resulting in poor performance due to inhibited electron transport through the catalyst layer to the OER active sites. In ionomer environments, the electronic conductivity is further stifled, which could be inhibiting the transition from the insulative Ni-Fe-based oxide to the highly electronically conductive NiFeOOH structure. Accordingly, the electronic conductivity of the catalysts appears to play a more significant role than previously understood for pure water AEM electrolysis.

Non-PGM Catalyst Restructuring

To further investigate the catalysts and their relationship with the ionomer, surface analysis was conducted via ex-situ XPS. Using XPS, information about both the ionomer and the catalyst can be accessed simultaneously. By analyzing the binding energy peaks of carbon, nitrogen, the relevant metals (Ni, Fe, Co), we can determine the amount of metal present at the surface, the oxidation state of those metals, and the extent to which oxidation of the carbons in the ionomer has occurred. Non-PGM OER catalysts are dynamic; Ni, Fe, and Co-based oxides will restructure during operation to the more active oxyhydroxide phase. This restructuring is accompanied by metal sites dissolving and redepositing during oeration.[25,30,32] Exchange of metals from the catalyst bulk into the ionomer layer before redepositing may result in the physical blocking of ionomer charge groups, therefore inhibiting the free movement of OH^-. Removal of catalyst material through dissolution may also result in detachment of the ionomer from the catalyst surface, also hindering the OER at the catalyst active sites. However, it is unclear exactly how restructuring can affect the stability of the ionomer or membrane in AEM systems. XPS surface analysis was performed on the catalyst layer (on a gas diffusion layer support) before and after operating in the electrolyzer conditions at 500 mA cm^{-2} for 20 h. A summary of the surface changes for the mixed metal catalysts is shown in Figure 12.

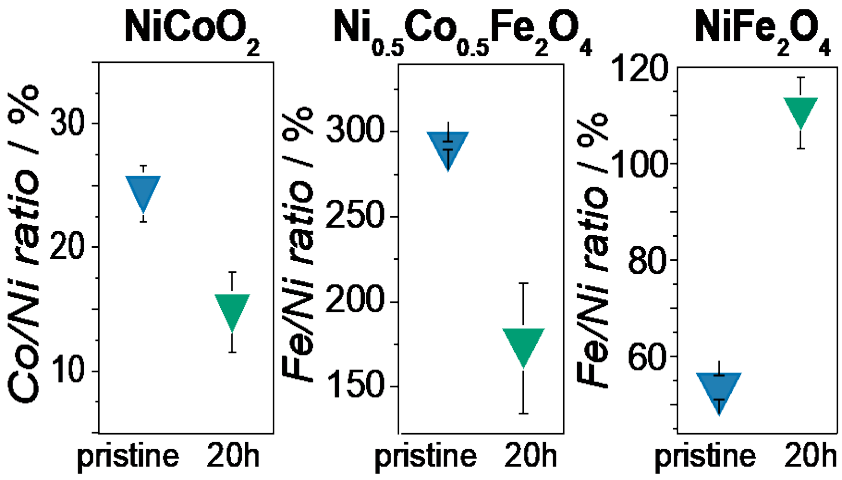

Figure 12. Non-PGM metal structure pre-and post-operation in AEM for 20 h at 500 mA cm^{-2}.

Quantitative constituent analysis of metals present at surface of catalyst for mixed-metal catalysts. Sample size n=3; data presented with mean as markers and standard deviation as error. Figure adapted with permission; collected and processed 2022 by Raina Krivina.[23]

The results show that all the mixed-metal catalysts undergo significant restructuring during operation, causing dissolution of certain metals, which then redeposit at the surface of the catalyst layer. The worst catalyst for activity and durability, $NiFe_2O_4$, experiences the greatest change in metal composition at the surface, with the percent of Fe to Ni at the surface, on average, doubling from 54% to about 110%.[23] This may indicate that Fe is dissolving into solution during use, forming an anionic Fe species that is unable to cross through the membrane to the cathode due to the influx of OH^- and the ionic selectivity of the membrane, resulting in eventual redeposition onto the outermost catalyst surface. $Ni_{0.5}Co_{0.5}Fe_2O_4$ and $NiCoO_2$ show that Ni is dissolving and redepositing at the surface, although Fe is likely also redepositing for $Ni_{0.5}Co_{0.5}Fe_2O_4$. For $Ni_{0.5}Co_{0.5}Fe_2O_4$, typically the second-worst performing catalyst in electrochemical testing, the restructuring appears greater, starting with a surface iron to nickel ratio of 290% and decreasing to 180% after operation, resulting in a layer of redeposited nickel covering the cobalt and iron.[23] The least amount of change is seen in the best performing mixed-metal catalyst, $NiCoO_2$, which

was tested for its cobalt to nickel ratio as iron was not present. This catalyst experienced some restructuring, going from a 24% cobalt to nickel ratio to a 15% ratio after operation, therefore forming a nickel layer on the outermost catalyst surface.[23] Co is known to be highly stable under OER conditions, therefore it is likely being covered at the surface by nickel, which could lead to the blocking of active sites and preventing the formation of the oxyhydroxide structure at the surface. These findings help explain the lower activity and durability of mixed-metal catalysts in AEM conditions, however, further investigation of each system would be necessary to understand the exact dissolution and redeposition processes occurring, and how they affect the stability of the ionomer.

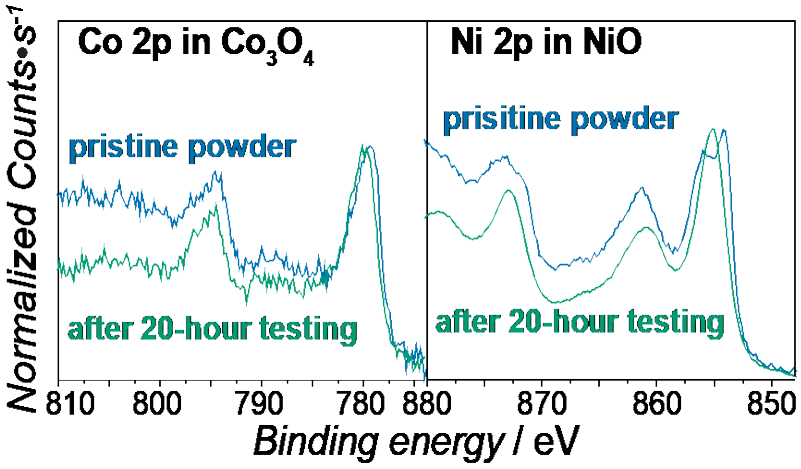

Figure 13. XPS spectra of 2p orbitals for Co of Co3O4 and Ni of NiO.

Non-PGM metal structure pre-and post-operation in AEM for 20 h at 500 mA cm^{-2}. Figure adapted with permission; collected and processed 2022 by Raina Krivina.[23]

The single metal oxide catalysts, NiO and Co_3O_4, were both analyzed for the binding energy and shape of peaks, shown in Figure 13. No changes to the crystal structure of Co_3O_4 are observed after operation, as exhibited by the almost identical Co 2p orbital peaks shown at a binding energy of approximately 780 electron volts (eV). This peak corresponds to the Co_3O_4 configuration, and confirms that cobalt is stable during extended AEM testing conditions.[23] Cobalt

oxides are known to form a thin layer of oxyhydroxide during use, often below the resolution detectible by XPS, and is therefore likely thin enough no not cause disruptive interaction with the ionomer, explaining its low degradation rate during electrolyzer operation.[33] However, NiO is shown to restructure during use, resulting in a peak shift to a higher binding energy consistent with the binding energy of NiOOH, the oxyhydroxide form of the catalyst.[23,34] Transitioning to NiOOH is thought to have to same consequences as the mixed-metal catalysts, wherein some nickel is dissolving and redepositing at the surface.[23] This XPS data, in combination with the durability data shown in Figure 9, indicates that the changing structure of the catalyst causes inhibitory blocking of active sites and impeding OH^- transport, which results in an initial rise in voltage before stabilization. Furthermore, the mixed metal catalysts may experience this redeposition and surface disruption to a greater extent, causing a significant loss of performance early in the extended testing as the catalyst layer restructures.

Considering the above experiments, a few trends are present across all methods of catalyst analysis. For each evaluation (activity, durability, and conductivity) Co_3O_4 performs best out of all non-PGMs. Its high relatively conductivity allows more of the catalyst to be utilized for OER reactions, increasing activity. Previous research has indicated that Co_3O_4 forms a highly OER active skin layer (CoOOH) in alkaline conditions that forms as a result of the oxide electrochemistry changing at potentials above 1.15 V.[33] However, any restructuring of Co_3O_4 during AEM electrolyzer operation is minute enough to appear to cause negative interactions with the ionomer. Lower performing catalysts were found to be those with mixed-metals and containing iron, which experience significant dissolution and redeposition. Their low conductivity likely contributes to poor activity, as catalyst material may not be readily accessible to perform OER.

Furthermore, interactions with the ionomer as a result of redeposition may be blocking the transport of OH^- or causing poor connectivity between the catalyst surface and the ionomer.

Polymer Degradation.

To better understand the role of ionomer degradation in the observed total cell voltage losses, NMR testing was conducted for all catalysts pre- and post-operation. As mentioned previously, NMR can provide information about the chemical environment of protons in a sample, and whether that environment has changed due to degradation before and after operation in an AEM electrolyzer.

Samples dissolved in d6-DMSO for testing via NMR spectrometry included the following: pristine membrane (never hydrated), spray-coated pristine and used electrodes for each catalyst (NiO, $NiFe_2O_4$, IrO_2, Co_3O_4, $NiCoO_2$, $NiCoFe_2O_4$, and PtBlk). TFA was added to all relevant samples to bind with any water left in the sample, causing the water peak to appear at a higher chemical shift and therefore out of our range of interest. The results from IrO_2, Co_3O_4, $NiCoFe_2O_4$, and $NiFe_2O_4$ represent the findings of all catalysts and are the only four discussed here for simplicity. Having a confirmed reference is important when conducting NMR testing on polymers because the resulting spectra can be very complex and convoluted, therefore difficult to decipher minute changes to the structure. For this reason, the literature standard NMR spectrum and known structure of the PiperION TP-85 ionomer used for this project is included (Figure 6[13]).

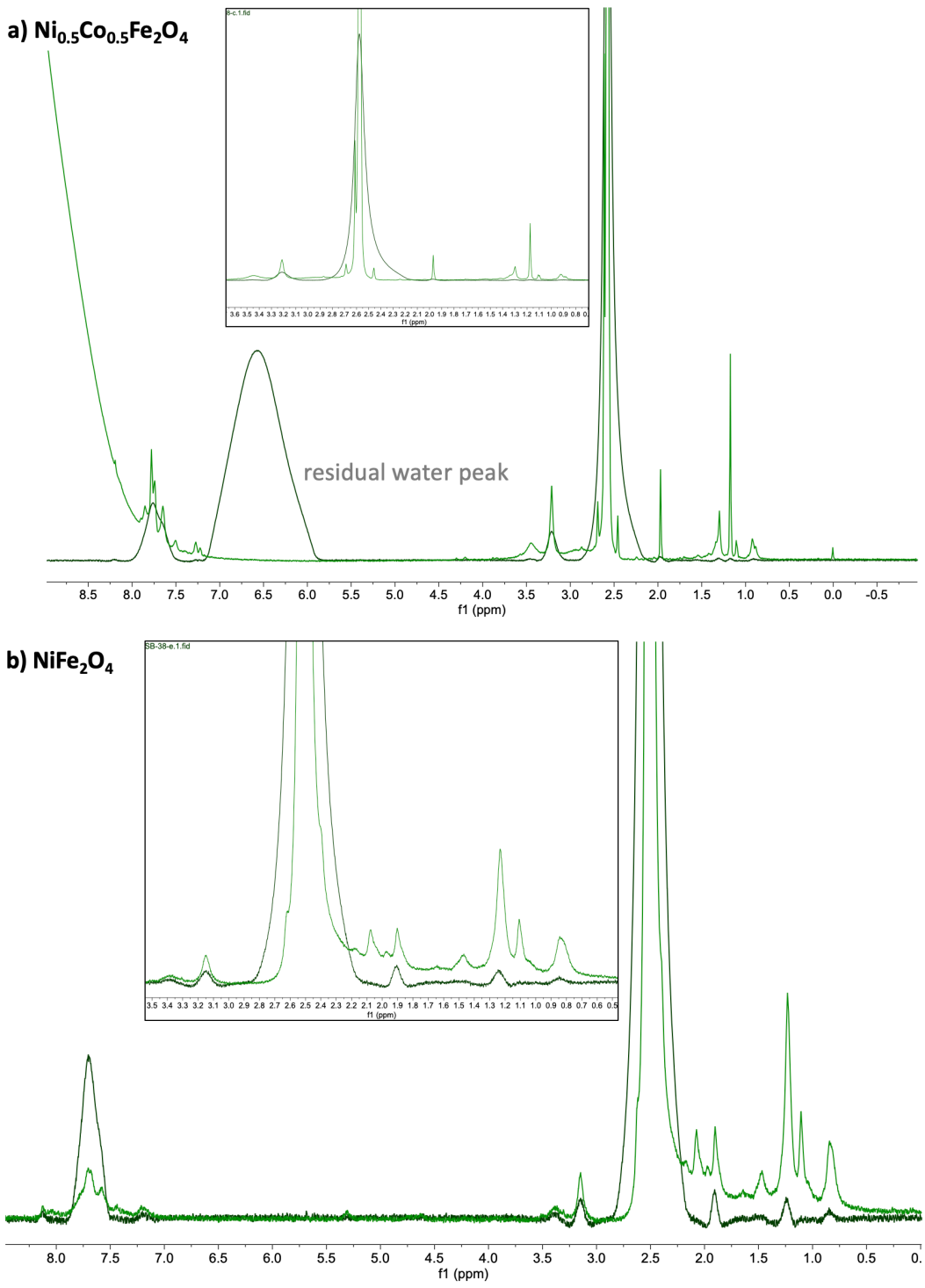

Figure 14. Hydrogen NMR spectra for iron-containing mixed-metal catalysts

a) $Ni_{0.5}Co_{0.5}Fe_2O_4$ and b) $NiFe_2O_4$, Dark green spectra from pre-operation sample, light green spectra from post-operation sample in AEM for 20 h at 500 mA cm^{-2}. Collected 2021.

Figure 14 displays the two spectra with testing optimized conditions that held the most significant information. It should be noted that proton integration could not be calculated due to substantial peak broadening and overlap, therefore the height of the peaks relative to each other is not significant. Instead, we looked for new peaks or disappearing peaks that formed during electrochemical use that might signify loss or gain of new organic species, therefore degradation in the ionomer. For both Co_3O_4 and IrO_2, no significant changes occur before and after the 20-hour electrochemical testing and the NMR spectrum reflects the literature standard. However, IrO_2 has been shown to cause significant ionomer degradation due to its high oxidizing potential.[23] Therefore, it is likely that during the sample preparation of used ionomer for NMR testing, some products of degradation could be lost, and would not be shown on the spectra above.

Both nickel-iron compounds, shown in Figure 14a and b, do show a noticeable addition of peaks in the 2.25 - 0 ppm range. This change in ionomer supports the hypothesis that significant structural changes to and redeposition of the catalyst layer has a degradative effect on the ionomer and may be representative of the low performance and low stability seen in these two catalysts compared to the others tested. While nuclear magnetic resonance spectroscopy suggests that the extent of polymer degradation varies with each catalyst used, further experimentation must be conducted in order to deconvolute the interactions between specific metals and the charged polymer structure. As seen, available NMR spectra are non-integratable for specifics of their hydrogen ratios, making them difficult to compare directly with each other.

Summary

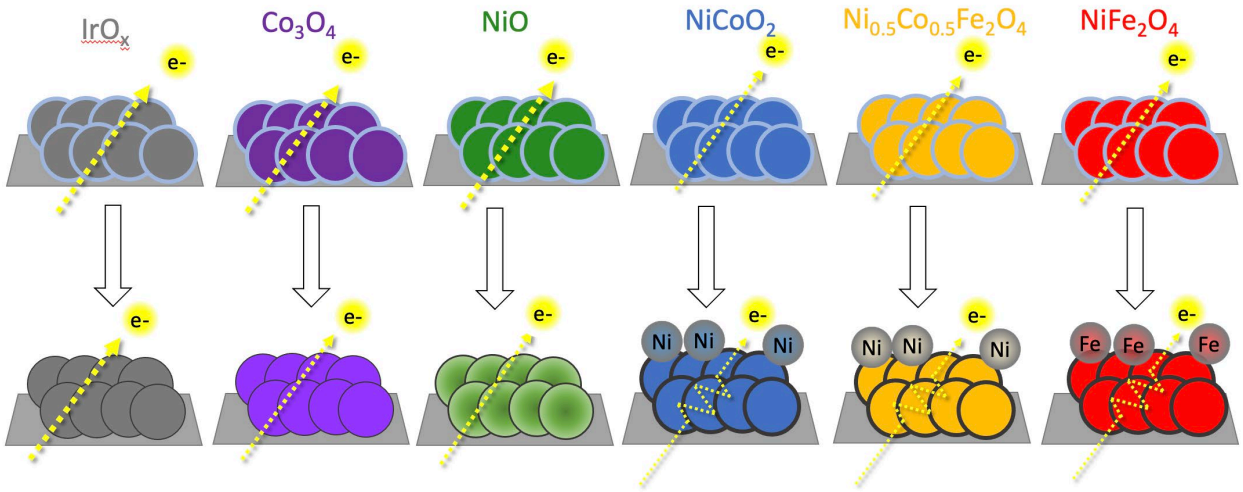

Figure 15. Visual summary of possible catalyst fates before and after operation in AEM for 20 h at 500 mA cm^{-2}.

Light blue represents pristine ionomer, dark brown represents degraded ionomer, light gradient represents transition to $O_x(OH)_y$ form (NiO), and redeposited metals appear on catalyst surface (Ni and Fe). Extent of ionomer degradation, electron movement, metal redeposition, and resistivity arbitrary and purely for illustrative purposes.

The goal of this chapter was to better understand trends in the activity and durability of five commercially available non-PGM metal oxide catalysts in an industrially relevant AEM system. Through the use of electrochemical testing in an AEMWE and three-electrode half-cell, compressed pellet conductivity, XPS, and NMR analysis, we were able to elucidate some of the key processes contributing to catalyst performance. It was found that catalyst electrical conductivity correlated directly with electrolyzer performance, with IrO_2 displaying the greatest activity and stability in an AEM electrolyzer. Co_3O_4 and NiO, the single metal catalysts, were consistently following IrO_2 regarding performance and durability, displaying, respectively, the second and third best performance in cyclic voltammetry testing (Fig. 10), stepped chronopotentiometry (Fig. 8), durability testing (Fig. 9), and conductivity (Fig. 11). The lower performance of NiO can be attributed to disruptions in the catalyst-ionomer interface when NiO

transitions to NiOOH under applied oxidative conditions, as found by XPS, as well as lower electronic conductivity that limits access to active sites. While cobalt oxides have been found to form a hyper-thin oxyhydroxide "skin", this evolution did not negatively impact the performance or stability of its long-term performance according to our testing. Co_3O_4 showed superior electric conductivity, allowing it to remain both active and stable throughout extended testing conditions.

The poor-performing catalysts were those of mixed-metal constitution, $NiFe_2O_4$, $NiCoO_2$, and $NiCoFe_2O_4$, likely due to their low relative electronic conductivity (Fig. 11) and significant surface reconstruction (Fig. 12). Poor electronic conductivity inhibits the movement of electrons to active sites, therefore decreasing OER activity. Metal dissolution and redeposition in these systems may result in the formation of a resistive redeposited layer on the surface of the catalyst, contributing to further voltage losses (Fig. 15).

Isolated performance experiments like the ones above help to reveal trends in catalyst behavior used to inform industrial standards as well as future research on OER catalysis. Our findings up to this point indicated that Co_3O_4 showed the greatest promise as a competitive catalyst for expensive and rare IrO_2 in both activity and durability in relevant AEM conditions. For this reason, Chapter Three will focus on a more in-depth exploration of commercially available cobalt oxide catalysts for AEMWE systems.

Chapter Three: Investigation of Cobalt Oxide Catalysts (2022-2023)

Background

Evidence of Cobalt Stability

Cobalt oxides have recently garnered interest in electrochemical communities seeking solutions for OER catalysis due to their long-term stability and high activity.[23] It has been shown that, for thin applications of spinel cobalt oxide (Co_3O_4), a hyper-thin oxyhydroxide layer will develop at potentials above 1.15 V in liquid alkaline conditions, and that this layer is directly proportional to the increased activity of the catalyst for OER.[33] For high-loading methods, which is needed for current AEMWE systems, cobalt oxide has shown an increase in activity with increased catalyst loading.[25] These studies agree with the findings of Chapter One, which indicated that the high activity of Co_3O_4 was due to its high electronic conductivity.

Because of cobalt oxides promising performance in pure water AEM systems, we further investigated five different commercially available cobalt oxide catalysts with varied diameter sizes and crystal structures to better understand the properties that make cobalt a successful catalyst for OER in alkaline conditions. The catalysts tested in this chapter are IrO_2 (for baseline reference), Co_3O_4 30-50nm diameter, Co_3O_4 10-30nm diameter, Co_3O_4 15 nm, Co_2O_3 50nm, and CoO 50nm. Co_3O_4 30-50nm is the same catalyst structure and size that was tested in Chapter One.

Results and Discussion

Assessment of each catalyst was completed using various techniques including three-electrode half-cell measurements in 1M KOH, electrolyzer testing in pure water, and conductivity measurements in the presence and absence of ionomer. For this chapter, the same cathode catalyst and membrane/ionomer, Pt Black and PiperION TP-85, respectively, were used throughout all testing. Three-electrode testing included both cyclic voltammetry for activity in liquid electrolyte conditions as well as capacitance testing to help determine the effects of ionomer on the activity

and surface area of the catalyst. Electrolyzer testing was used again to understand catalyst its activity and long-term durability in the absence of supporting alkaline electrolyte. Conductivity was performed in a pellet press to understand the electronic conductivity of each catalyst tested, both as dry pristine catalyst powder and in the form of a dried ink containing thoroughly dispersed ionomer. This chapter aims to illuminate the properties that make a successful cobalt oxide catalyst for OER in industrial settings and to inform future studies on cobalt oxide catalysts.

Co_xO_y Conductivity

The first measurement taken of each catalyst was that of conductivity, due to the significant role it played in the performance of Chapter Two non-PGM catalyst performance. Activity in AEM electrolysis scaled with electronic conductivity of the dry catalyst purity, but the effect of ionomer on catalyst electronically conductivity was not directly measured using the same method of compressed pellet conductivity. The ionomer is electronically insulative and may disrupt catalyst connectivity when dispersed throughout the ink, but the extent to which ionomer effects electronic conductivity may be different for catalysts of varying crystal structure and size. Therefore, we tested both dry powder and ink film electrical conductivity to elucidate the relationship between ionomer presence and electrical conductivity. The results for both powder-only and ink conductivity are shown in Figure 16. IrO_2 was not tested again as it was previously found to be highly conductive and comparable with bare metal.[23]

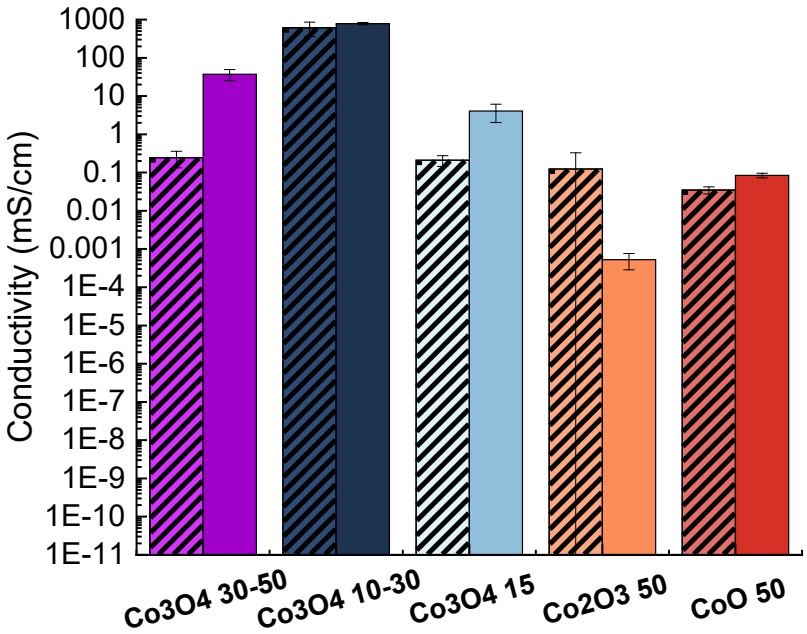

Figure 16. Conductivity of ionomer-free and ionomer-containing environments for each catalyst.

Processed data from chronoamperometry of catalyst powder in pellet press at 1000 psi. Sample size n=3; data presented with mean as bars and standard deviation as error. Striped bars represent catalyst powder while solid-colored bars represent catalyst ink with ionomer. Collected 2023 with the help of Willow Thompson.

According to Figure 16, the electronic conductivity is typically lower for ionomer-containing ink than for powder only. This is expected, as the ionomer is ionically conductive for anions, but electronically resistive (Figure 4b).[13,15,23] The exception to this rule is Co_2O_3 50 nm, which shows greater conductivity when in an ionomer environment. This may be due to an increase in connectivity between particles when dispersed and applied in liquid layers to the stainless-steel pellet before being tested. However, this catalyst also exhibited the lowest conductivity overall, with the greatest amount of error present, so this may be a result of error and could be tested again for a more rigorous understanding of this unexpected relationship in the future.

All other catalysts behaved as expected, with Co_3O_4 10-30 nm exhibiting the greatest electronic conductivity in both conditions. This may be due to its smaller and mixed size of nanoparticles, ranging from 10-30 nm in diameter, which have a high surface area to volume ratio and may more effectively pack together for greater electronic connectivity. Our baseline cobalt oxide, Co_3O_4 30-50 nm, has the second-best conductivity as a powder, but this conductivity is significantly hindered in an ionomer environment. Co_3O_4 15 nm shares similar conductivity with the rest of the spinel configuration sizes, being only slightly less conductive than Co_3O_4 30-50 nm but indicating a large resistive effect when in the presence of ionomer. Both non-spinel type catalysts have lower conductivity and larger diameter than their spinel counterparts. The lesser surface area per volume ratio may lead to poor connectivity, or the crystal structure itself may be less conducive to electron transport.

Co_xO_y Activity and Durability

After the electronic conductivity was determined for each catalyst, activity and durability was tested in both AEMWE and half-cell liquid electrolyte conditions. For three-electrode half-cell measurements, the activity was determined via cyclic voltammetry for 8 distinct cycles, and the data for the first cycle and last cycle is shown in Figure 17. The first cycle of IrO_2 from 2021 was included in Figure 17a for reference.

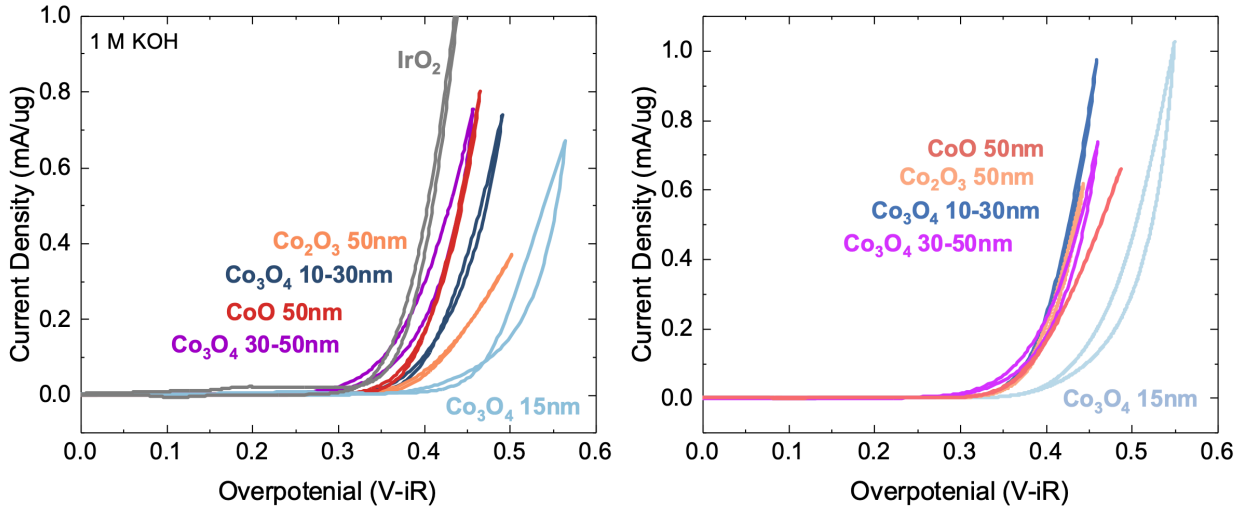

Figure 17. Cyclic voltammetry in three-electrode half-cell with 1M KOH electrolyte. a) first cycle b) last (8^{th}) cycle for each catalyst

Sample size n=3; data presented as average of three first cycles for each catalyst. Richer colors represent first cycle while pale colors represent last cycle. Voltage has been corrected to overpotential by subtracting system resistivities (*iR*). Collected 2022.

The catalyst with the greatest first cycle activity is still IrO_2 (Figure 17a). Following IrO_2 is Co_3O_4 30-50 nm, having similar performance to what was found in Chapter One, Figure 10. CoO 50 nm follows Co_3O_4 30-50 nm in liquid electrolyte conditions during the first cycle. Co_3O_4 10-30 nm is the third most active, followed by Co_2O_3 50 nm and then Co_3O_4 15 nm.

After catalysts have been operated, catalyst activity changes drastically (Figure 17b), we with almost all the catalyst activities grouping together at the same overpotential and now matching the activity of the baseline catalyst, Co_3O_4 30-50 nm. This change in activity indicates that catalysts may be undergoing structural changes during cycling after exposure to voltage and oxidative conditions and evolving to a similar crystal structure as Co_3O_4.

Activity was also tested for the cobalt oxides and iridium in pure water electrolyzer conditions, shown in Figure 18.

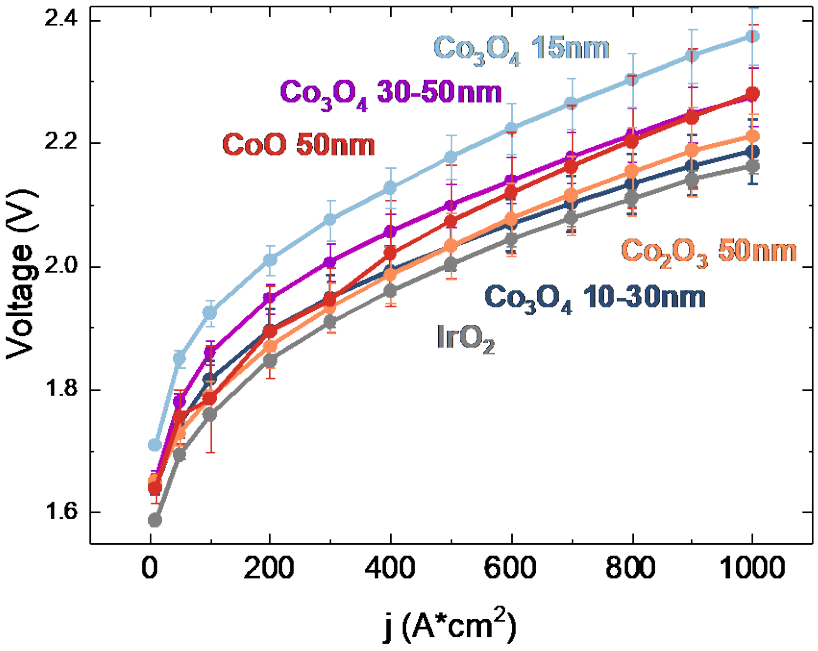

Figure 18. Stepped Chronopotentiometry polarization curve in AEMWE at 57 °C.

Sample size n=3; data presented with mean as points and standard deviation as error. Collected 2023.

Again, the activity trends seen in the electrolyzer were found to mostly match the electronic conductivity testing. All catalysts exhibit similar performance at low current, except for Co_3O_4 15 nm, which performs notably worse across all currents. Co_2O_3 50 nm performed better than expected, compared to three-electrode and conductivity measurements. This evidence further supports the findings in Chapter One indicating catalysts are not able to restructure in pure water to the same extent as in supporting electrolyte, as all catalysts achieved similar activity after cycling in KOH but show very different performance in a pure water system, mostly trending with dry electronic conductivity. The improved performance of Co_2O_3 may indicate it undergoes structural evolutions more easily than other Co catalysts. The electrolyzer testing also included long-term durability testing of each catalyst at 500 mA cm^{-2} for 20 hours at 57 °C, displayed in Figure 19.

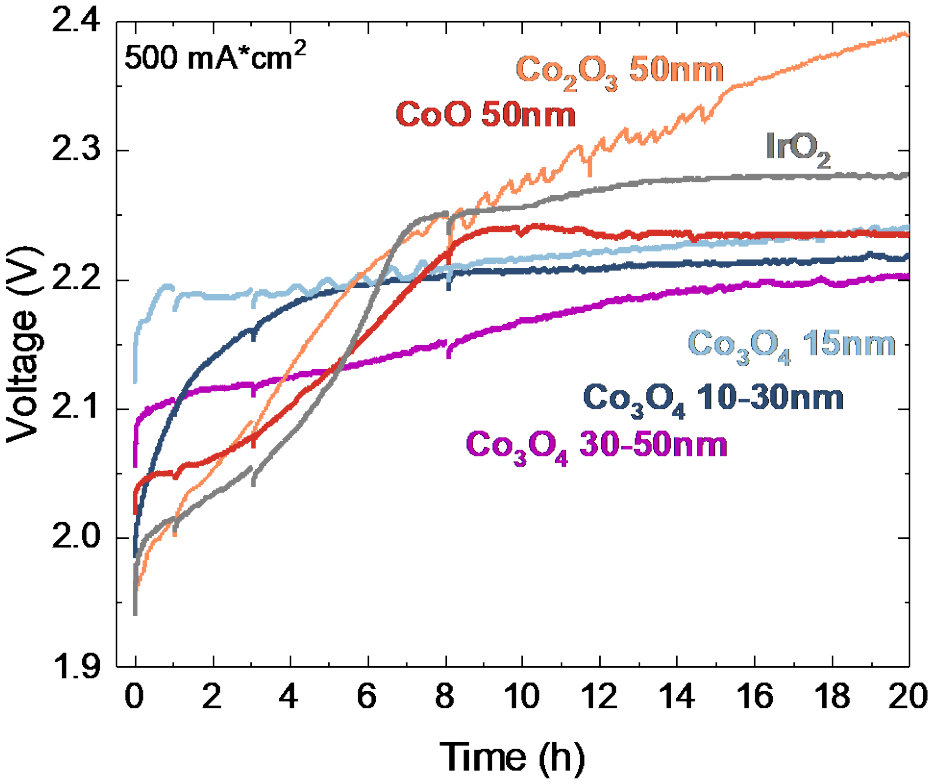

Figure 19. Extended Chronopotentiometry at 500 mA cm^{-2} for 20 h in AEMWE at 57 °C.

Sample size n=1; data presented as one extended measurement for each catalyst. Collected 2023.

Durability testing for cobalt oxides indicates two main stages of performance. The first stage, occurring from approximately 0 to 8 hours of continuous testing, signifies significant ionomer degradation that can be seen as worsening performance for most catalysts. This is especially true for IrO_2, which rapidly degrades before stabilizing at about 2.25 V shortly before hour 8 of testing, and CoO 50 nm, which experiences a similar pattern of degradation before leveling off at 2.2 V. Manufacturing processing of the ionomer was altered between the data collection of Chapter Two and Chapter Three, resulting in worse performance in Chapter Three. Ionomer degradation trends with voltage, therefore the higher operating potentials are believed to be the reason for the worse durability of IrO_2 seen here.

The restructuring of the non-spinel forms of cobalt oxide may further contribute to rapid initial degradation. Similar to the shift in activity seen during half-cell testing (Fig. 17), Figure 19 indicates that Co_2O_3 50 nm and CoO 50 nm are restructuring during the first 8 hours, causing interference with the ionomer, before stabilizing to a similar activity as Co_3O_4 30-50 nm at around 2.2-2.25 V. In the case of Co_2O_3 50 nm, it's possible that initial restructuring, as well as having the highest inherent resistivity, results in continued degradation and loss of performance, as opposed to stabilization. Instability starting at hour 8 is the result of a water pump failure, which may have any contributed to the loss of activity. Co_3O_4 15 nm also experienced some water pump complications beginning at hour 3 that were fixed by hour 8.

It has previously been shown that Co_xO_y (non-spinel) catalysts will reconfigure irreversibly to Co^{3+} forms during OER.[35] Conversely, Co_3O_4, which is already consisting of Co^{3+} and Co^{2+}, retains its crystal structure under OER potentials.[35,36] This charge shift is separate from the reversible oxyhydroxide layer forming on Co_3O_4, which results in a transition to Co^{3+}/ Co^{4+} in a $Co^{+3/4}O_x(OH)_y$ amorphous layer on the surface of the catalyst. It is still unclear why OER is coupled with a transition to the $Co^{+3/4}$ oxidation state, although it has been hypothesized that bulk water nucleophilic attack, a necessary step in the formation of oxygen gas via electrolysis, occurring at the terminal oxygens of the catalyst layer causes the redox transition for the bonded cobalt.

Considering the conductivity from Figure 16, it may be possible to deconvolute the poor performance of Co_3O_4 15 nm compared to the other catalysts, despite its starting spinel crystalline structure. It shows the lowest initial conductivity of the spinels, as well as poor catalytic activity at low current density that is apparently inherent to the catalysts surface area to volume ratio. Being the only spinel with no variation in nanoparticle size from the manufacturer, the connectivity and

assembly of the crystalline structures could be hindered by the lack of variability, as illustrated in Figure 20. Smaller particle size may also be more susceptible to disruption by the ionomer, as particles may disperse more thoroughly with ionomer in the ink solution.

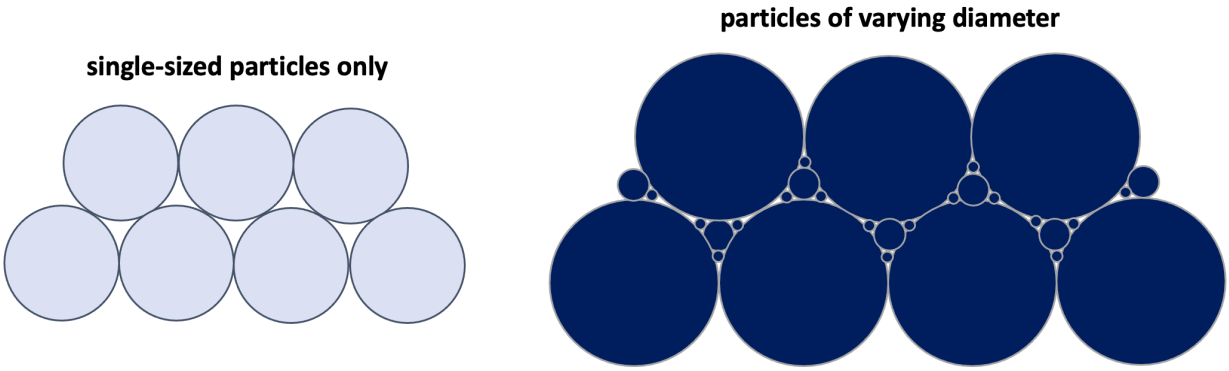

Figure 20. Illustration of particle connectivity for variable-diameter nanoparticles and single size particles.

Lower activity seen in Co3O4 15nm may be the result of gaps in connectivity due to uniform particle sizing, compared to in Co3O4 10-30nm and 30-50nm. Size of particles arbitrary and used for illustrative purposes only.

Unlike Co_2O_3 and CoO, Co_3O_4 15 nm has poor activity and may not have the opportunity to restructure during OER conditions. The former two catalysts indicate efficient restructuring to the active $Co^{+3/4}$ oxidation state in the half-cell activity measurements (Figure 17) over 8 cycles, while Co_3O_4 15 nm remains the worst performing catalyst during the first and last cycle due to its inherently poor OER abilities and inability to restructure. This exact trend may not be represented for extended durability testing due to the degradative interactions of restructuring catalysts and the ionomer. If significant restructuring is occurring, this could damage the ionomer, the effects of which would be more noticeable in AEMWE, where the ionomer is necessary to facilitate the movement of ions to the active sites of the catalyst. That may explain why the activity of all catalysts except Co_3O_4 15 nm are comparable after 8 cycles in liquid electrolyte.

Co_xO_y Capacitance

Between cycling in the three-electrode half-cell, capacitance was measured by cycling from 0.0 to 0.3V, below OER potentials, while measuring current response over the frequencies 5, 10, 20, 100 mV s^{-1}. The current at a given voltage can then be measured and plotted against the scan frequency, wherein the following slope is the capacitance of the catalyst layer. This is representative of the electrochemically active sites in the catalyst. Capacitance measurements were repeated for each catalyst with new electrodes of increasing catalyst loading, via spin coating ink dispersion, as measured by the quartz crystal microbalance. By doing so, catalyst capacitance can be plotted verses loading to understand catalyst electronic conductivity with respect to mass loading.

Theoretically, it would be expected that catalyst capacitance would increase linearly with increased material, as there should be more material through which to store and transport charge. When considering the addition of electronically resistive ionomer to the ink, this linear slope may eventually plateau provided high enough loading. At the high ionomer concentration necessary for stable AEM electrolysis, the electronically insulative ionomer will disrupt electronic movement through the catalyst layer, resulting in no increase in activity with increased loading. The results of this experiment are shown in Figure 21.

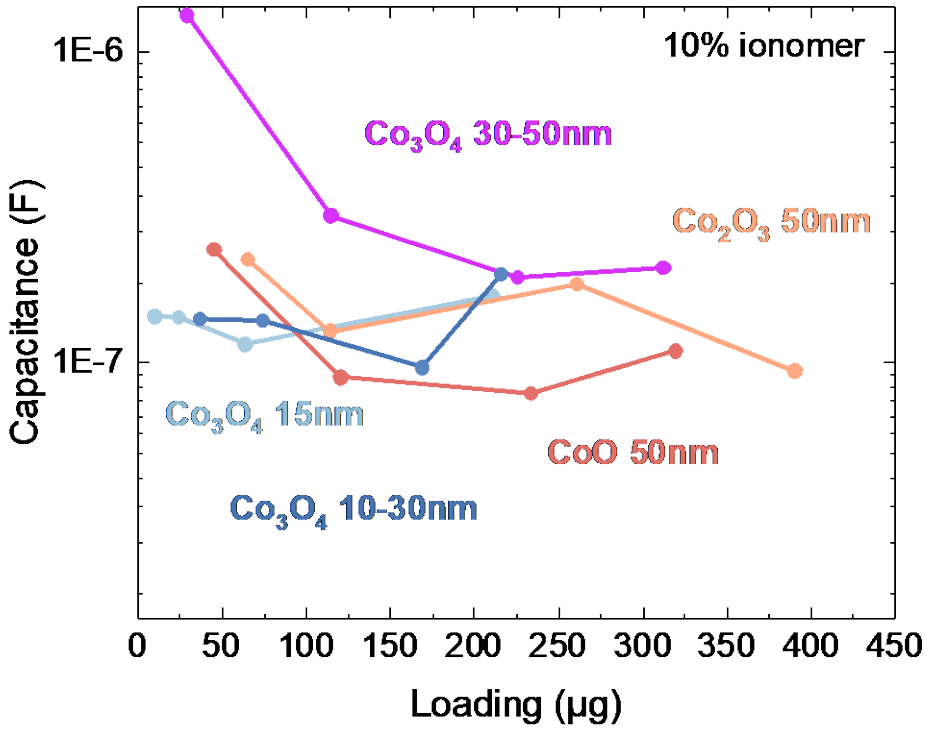

Figure 21. Capacitance vs loading for all cobalt oxides.

All inks contain ionomer and were dispersed onto the quartz crystal microbalance via spin coating of 1 layer, 2 layers, 4 layers, and 6 layers as shown by the data points. Collected 2022.

Shown in Figure 21, all catalysts exhibit a roughly flat relationship between increasing catalyst ink loading and capacitance. Therefore, the electronically insulative properties of the ionomer are significantly impeding electrical conductivity for all catalysts. While some catalysts, such as Co_3O_4 30-50 nm appear to decrease as catalyst loading is increased, this trend cannot be confirmed due to the lack of triplicate measurements taken. Currently, it is unknown if this apparent trend is due to noise or error, with the actual slope being closer to zero, or if additional catalyst ink does decrease capacitance for Co_3O_4 30-50 nm. Given that other catalysts exhibit zig-zagging lines of increasing and decreasing capacitance, replicate testing would be necessary to

fully understand the relationship for each catalyst between loading and capacitance in the presence of ionomer.

For the best and worst performing catalysts in liquid electrolyte testing, Co_3O_4 30-50 nm and Co_3O_4 15 nm, the experiment was repeated but without ionomer in the ink. The results are compared to the initial ionomer experiment for Co_3O_4 30-50 nm and Co_3O_4 15 nm in Figure 22.

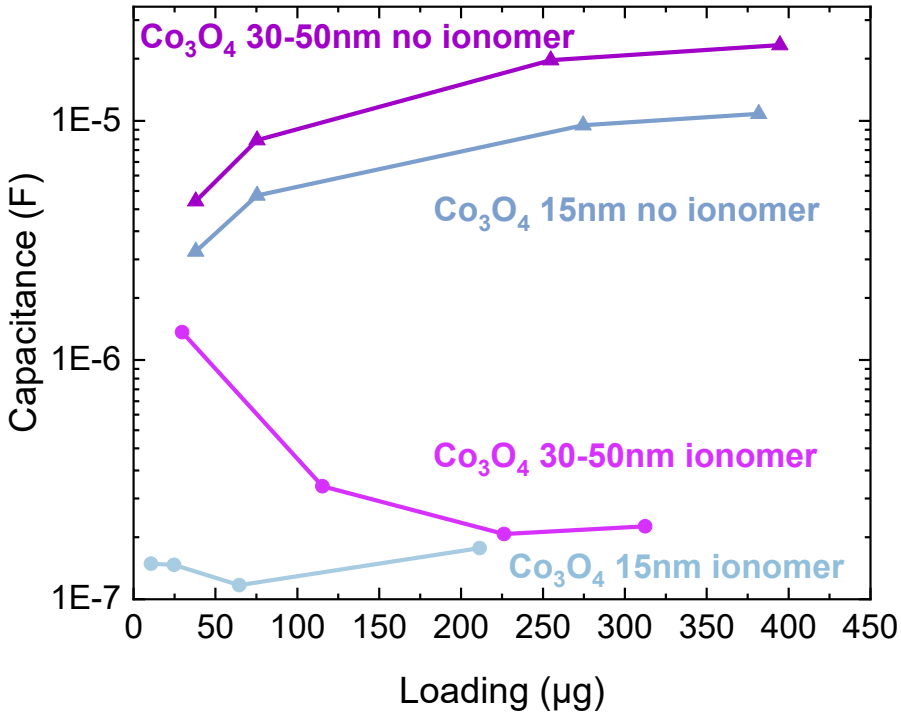

Figure 22. Capacitance vs loading for ionomer and non-ionomer environments of Co_3O_4 30-50nm and Co_3O_4 15nm.

Richer colors represent an ionomer-free environment while pale colors represent an ionomer-containing environment. Collected 2022.

The ionomer-free data more closely exhibits the expected behavior of increasing linearly and then plateauing with increased catalyst loading, as shown by the positive slopes in Figure 22 for those experiments. This data indicates that the electrically resistive ionomer dominates the electronic conductivity of the catalyst layer. Physically, this means that only the outer layer of the catalyst

can be viewed as conductive, as bulk internal material largely is inaccessible for electrons to move freely.

Summary

The goal of this chapter was to better understand the high performance of cobalt oxides as OER catalysts in pure water AEM devices. To do so, we explored their activity in three-electrode liquid electrolyte conditions as well as in an AEMWE, durability testing in extended AEM conditions, loading-dependent capacitance measurements, and electronic conductivity in ionomer-containing and non-ionomer catalyst layers. In doing so, we found that non-spinel forms of cobalt oxide catalyst undergo restructuring during oxidative potentials to form a more active state. In liquid electrolyte conditions, this restructuring causes an increase in activity to match the activity of the best performing cobalt oxide, Co_3O_4 30-50 nm. However, in a pure water AEM testing, the same reconfiguration results in voltage degradation, likely due to disruptions in the ionomer-catalyst interface and consequential loss of activity to varying extents. Co_3O_4 15 nm performs poorly as a catalyst for OER, possibly due to uniform diameter particles causing less connectivity for electron transfer than the non-uniform sizing of Co_3O_4 30-50 nm or 10-30 nm. Capacitance data indicates that the presence of ionomer has a significant effect on catalyst performance, decreasing catalyst layer electronic conductivity. Capacitance does not increase with loading, possibly indicating that only a thin layer of active catalyst is available for OER in pure water AEM systems.

Conclusions and Future Directions

In the present study, we have revealed critical trends in catalyst performance and activity relating to the electronic conductivity of metal oxides, the extent to which they restructure under oxidizing potentials, and their interactions with the ionomer. Chapter One outlines the known relationship between anion exchange ionomer conductivity and stability and discusses common ionomer degradation pathways. It was found that quenching any materials containing ionomer or the membrane itself in a Cl^- solution inhibits nucleophilic Hoffmann Elimination of the polymer by OH^-. Thanks to these results, quenching is now a common technique employed to reduce degradation during preparation, use, storage, and analysis.

In Chapter Two, five non-PGM catalysts were analyzed for activity in alkaline electrolyte, performance, and durability in AEMWE, electronic conductivity, surface restructuring via XPS, and polymer degradation using NMR. Results indicate that IrO_2 exhibits the highest catalyst electronic conductivity, as well as the best performance in basic electrolyte and AEMWE. IrO_2 was also found to substantially oxidize the ionomer at the surface of the catalyst, but the electronic conductivity of the catalyst allowed for retention of OER activity. Co_3O_4 was the second most conductive and performed accordingly in AEMWE, seemingly causing less oxidation of the ionomer and showing no indication of dissolution or restructuring beyond the likely formation of a thin oxyhydroxide layer imperceivable by XPS and therefore not disruptively interacting with the ionomer. NiO indicated mediocre performance which is attributed to its restructuring to the NiOOH phase, causing redeposition of Ni onto the catalyst surface, blocking active sites and otherwise hindering OH^- movement. Mixed-metal non-PGMs $NiFe_2O_4$, $NiCoO_2$, and $NiCoFe_2O_4$, all performed poorly in AEMWE, despite previously shown high activity in alkaline liquid electrolyte. This was found to be a result of low electronic conductivity and significant dissolution

and redeposition of Ni and Fe from the catalyst layer onto the catalyst surface, creating a resistive layer that impedes the necessary merging of electrons and OH^- at the catalyst active sites.

Chapter Three utilized the insights gained in Chapter Two to further explore the highest performing non-PGM catalyst, Co_3O_4. For this study, five more catalysts were chosen that encompassed a range of cobalt oxide crystal structure and particle size. The electronic conductivity, AEMWE performance and durability, liquid electrolyte activity, and capacitance were measured to reveal trends in cobalt oxide OER potential. Results show that conductivity is still an important factor in determining the AEMWE activity of cobalt oxides, however the size distribution of particles and the potential restructuring of Co_xO_y phases to $Co^{3+/4+}$ may play a more significant role than that found in Chapter Two. However, such restructuring also appears to exhibit negative interactions with the ionomer. It was also discovered that typical ionomer loading inhibits electrical conductivity of all cobalt oxide catalysts in alkaline electrolyte.

This work has led to the possibility of future research analyzing the surface and crystal composition of cobalt oxide catalysts via X-Ray diffraction (XRD) and XPS. Studying the cobalt systems presented here using these methods would provide insight into the charge of cobalt in the bulk and at the surface of the catalyst and could reveal insights on how the ionomer is affected by cobalt oxide restructuring. By working to resolve the complex dynamics of various non-PGM oxides with the anion exchange ionomer, AEMWEs can continue to develop and increase accessibility to green hydrogen fuel. Research in the field of low-cost oxidation catalysts for oxidation in pure water electrolyzers will only continue to gain importance as fossil fuels are phased out in exchange for environmentally benign energy alternatives.

Experimental

Catalyst Dispersions and GDL Coating. Pt black (high surface area, Fuel Cell Store) nanoparticles were used as the cathode catalyst for all trials. Co_3O_4, NiO, $NiCoO_2$, $NiFe_2O_4$, $Ni_{0.5}Co_{0.5}Fe_2O_4$ (all non-PGMs from US Research Nanomaterials, Inc.), and IrO_2 (Fuel Cell Store) nanoparticles were used at the anode. Cathode and anode ink solutions were prepared identically; for every 100 mg of catalyst, 0.5 g of H_2O was added, followed by 1.7 g of 2-propanol and 200 mg PiperION (TP-85, 5% w/w in ethanol) was added to yield the final 10 wt % ($w_{ionomer}/w_{catalyst}$) ink. Inks were then bath-sonicated (Branson 1510R-MTH or Branson 3510) at room temperature for a minimum of 1 h (Pt black, Co_3O_4, NiO, $NiCoO_2$, $NiFe_2O_4$, $Ni_{0.5}Co_{0.5}Fe_2O_4$) or 2 h (IrO_2) until fully dispersed.

Toray 090 carbon paper (Fuel Cell Store) and a stainless-steel mesh filter material (25AL3, Bekaert) were used as the cathode and anode GDLs, respectively. The GDL was taped to a hot plate set to 80 °C. Catalyst inks were sprayed onto the GDL materials using an airbrush (Testors, Aztek A2203, part of the "Amazing Airbrush" kit) and compressed N_2 at a pressure of 12 psi. A catalyst loading between 2.0 and 2.5 mg cm^{-2} was determined by mass difference. A thin layer (TP-85, 2.5% w/w in ethanol) of ionomer solution was sprayed on top of the catalyst layer to improve contact with the membrane.

Membrane Conditioning. PiperION (TP-85 40 μm, W7Energy) membranes were conditioned according to manufacturer instructions. The membranes were soaked in 0.5 M KOH (PiperION) for 48 h, replacing the solution with fresh KOH after 24 h. Membranes were stored in 0.5 M (PiperION) when not in use. . Due to apparent ionomer degradation occurring if ionomer is allowed to dry in the hydrated form, proper quenching of the catalyst coated GDLs using 3 M

NaCl or 1 M HCl is essential. For GDLs made to be stored for greater than 48 hours or prepared for testing not using electrochemical methods, GDLs were quenched directly after spray-coating procedure by submerging completely in 3 M NaCl solution for at least 1 hour, or until pH strip showed significant basification of the used quenching fluid (showing transfer of OH^- ion out of ionomer charge channels). For GDLs about to undergo electrolyzer testing (within 48 hours of spray-coating), quenching was suspended until after electrochemical testing. In both cases, GDLs are rinsed with 18.2 MΩ cm water after being removed from the quenching bath and allowed to dry in open air. Once properly saturated with chloride ions and dried, the GDLs are expected to remain stable indefinitely.

MEA Assembly. The serpentine flow fields can apply an uneven pressure to the relatively flexible SS GDL, so a sintered Ti plate was used as a rigid back support on both the cathode and anode side (400 μm thickness, Baoji Yingao Metal Materials Inc.). Gasket material (0.005 in. PET/PETE clear film, McMaster-Carr) was laser cut to an active area of 1 cm^2. Gaskets were added until they were flush with the GDL surface. The number of gaskets was determined by adding/ removing a gasket until maximum performance was obtained. The conditioned membrane was rinsed with 18.2 MΩ water for at least 10 s before assembly. Materials were assembled in the stack and a torque wrench was used to tighten the eight bolts to 67.8 N m.

Electrolyzer Operation. The electrochemical activity and long -term stability of the catalysts mentioned above were conducted using a pure-water fed electrolyzer cell in which 18.2 MΩ cm water was flowed to the cathode and anode at 500 mL min^{-1}. The anode water flow (carrying produced O_2) was recirculated in the system while the cathode water flow (carrying produced H_2) flowed into a chemical hood, degassed in a flask of 18.2 MΩ cm water, then recirculated back into the water tank. Temperature of the tank was maintained such that the

temperature in the electrolyzer cell was 56-58 C° and was monitored with a thermocouple inserted into the cell hardware. Once the cell temperature was stable, the MEA was conditioned by stepping the current from 100 mA cm^{-2} to 1 A cm^{-2} in 100 mA intervals, holding for 2 minutes at each step. This was followed by impedance testing, consisting of a frequency sweep ranging from 500 kHz to 200 mHz at 50 mA. Then, the cell was then held at 1 V to test for pinholes or other short-circuit pathways in the cell. The cell was brought back to 1 A cm^{-2} for 2 min to stabilize. The potential was then recorded, and the current was decreased in 100 mA cm^{-2} steps until reaching 100 mA, then further decreased to 50 mA and lastly 10 mA, measuring the potential for 10 s at each step to collect the JV (applied current vs volts) curve. The final JV curve provides the immediate activity of the catalyst being tested. For stability measurements, the cell was then held at 500 mA cm^{-2} for 20 hours. During stability testing, impedance data as described above was collected at the following intervals from starting: 1 hr, 3 hrs, 8 hrs, and 20 hrs. Data points taken directly after impedance testing, but before the current had restabilized to 500 mA cm^{-2} , were removed for clarity.

Polymer Analysis. Degradation of the ionomer and membrane materials was done via Nuclear Magnetic Resonance (NMR) in a Bruker 600 instrument. Samples for these tests consisted of both pure membrane as well as ionomer-coated catalysts, used and pristine. Samples were dried, then dissolved in deuterated dimethyl sulfoxide (d6-DMSO) by heating polymer and solvent on a hot plate set to 60 C° for 1 hour, then sonicating in a sonication water bath for 2 hours. If the ionomer was part of a catalyst-coated electrode and required extraction from the metal nanoparticles, the solution would then be centrifuged at 7500 rpm for 30 minutes or until metal particles were sufficiently separated from ionomer in solution. After the discovery of a significant water peak in the initial NMR scans, we began adding 5-10 from a micropipette of trifluoracetic

acid (TFA) to our samples before NMR testing. TFA binds to the water, resulting in downfield displacement away from polymer peaks therefore increasing the detail of our spectra.

Conductivity Measurements. To measure the conductivity of catalyst powders, approximately 200 mg of the powder were compressed between two stainless steel disks embedded in a plastic holder. An aluminum bar was placed above and below the disks to establish electrical contact, and copper wires connected the disks to a potentiostat. Plastic sheets were inserted between the aluminum bar and the disks to avoid any short-circuiting through the metal press. The powders were compressed to 23,000 psi in Chapter One, and 1,000 psi in Chapter Two. The thickness of the powder was determined by measuring the distance between the top and bottom of the steel disks using a digital micrometer and subtracting the thickness of the disks without catalyst powder. Polarization curves were generated by sweeping the voltage from −1 to 1 V at 1 V s^{-1}. The contact resistance was measured using the same method, but without the catalyst powder between the two disks. To prevent current overload during blank and IrO_2 measurements, the range was adjusted to −0.02 to 0.02 V at 10 mV s–1. As the measurement of IrO_2 matched the contact resistance, no value was reported for this catalyst. For all other catalysts, the resistance was obtained by fitting the current–voltage curve linearly. Before computing the conductivity using the equation $\sigma = l/(RA)$, where σ represents the electrical conductivity in S cm^{-1}, l represents the thickness of the catalyst powder in cm, R represents the measured resistance in Ω, and A represents the surface area of the disks in cm^2, the blank resistance was subtracted.

Conductivity measurements were taken under working conditions by repeating the experiment above using the previously made catalyst inks. Rather than test the dry catalyst powder, 3 drops of sonicated ink were drop-cast onto two aluminum pellets each and allowed to dry on a hot plate, ensuring the entire surface had dried before repeating the process for 6 layers or approximately

18-20 drops. They were then dried on a hot plate at 80°C for 15 minutes to remove any remaining water. After drying, the pellets were sandwiched together catalyst side facing in. The electrochemical tests conducted on the wet catalysts also followed the structure detailed previously for dry conductivity.

Testing of Catalyst Ink on Quartz-Crystal-Microbalance (QCM) Electrodes in KOH. The catalyst inks were prepared following the same procedure as for device testing and then spin-coated onto 5 MHz Au/Ti quartz crystals (Fil-Tech) at 3000 rpm and dried at 80 °C to obtain a loading of ≈22 μgMO cm^{-2} (normalized to exclude the mass of the ionomer) for Chapter One. For Chapter Two, additional layers of catalyst were added after drying on the hot plate by repeating the previous step, resulting in a loading of 10-400 μg (normalized to exclude mass of ionomer where appropriate). Cyclic voltammetry (CV) plots were obtained using a potentiostat (BioLogic, SP-200) in 1.0 M KOH with the working electrodes connected to the QCM controller (Stanford Research Systems QCM200) sweeping from 0.0 to 0.9 V for Chapter Two. Potentials in three-electrode modes were measured against a 1 m KOH Hg/HgO reference electrode (CH Instruments). Before the electrochemical measurements, the reference electrode was calibrated using a reversible hydrogen electrode (HydroFlex). During the QCM experiments, the electrolytes were either bubbled with high-purity N_2 or conducted in open air. All three-electrode electrochemical data were corrected for uncompensated series resistance (Ru), which was determined by equating Ru to the minimum total impedance in the frequency regime between 10 and 50 kHz, where the capacitive and inductive impedances are negligible, and the phase angle was near zero. In Chapter Two, all CV data was taken from only the QCM with one layer of catalyst, while subsequent layers were used solely for capacitance measurements.

The capacitance was calculated from the capacitance during cycling voltammograms in the potential range 0–0.3 V vs reference electrode and by varying the scan rate (5, 10, 20, and 100 mV s−1). The current at a given voltage (approximately 1.15 E vs RHE when current is positive) was measured and plotted against the scan frequency, wherein the following slope is the capacitance of the catalyst layer. This was repeated for each catalyst with new electrodes of increasing catalyst loading of 1 layer, 2 layers, 4 layers, and 6 layers ad described by the above spin coating technique. Lastly, catalyst capacitance in Farads was plotted verses loading in micrograms.

Supplemental Data. Data collected by lab members of the Boettcher lab played a significant role in the successful completion of this paper. Graduate researcher Raina Krivina PhD, graduate researcher Grace Lindquist, undergraduate researcher Nathan Stovall, and lab assistant Willow Thomspon played a significant part in the development and understanding of this project, as well as collection of data. Appropriate credit is provided in figure captions throughout the body of the paper.

Bibliography

(1) Ayers, K.; Danilovic, N.; Ouimet, R.; Carmo, M.; Pivovar, B.; Bornstein, M. Perspectives on Low-Temperature Electrolysis and Potential for Renewable Hydrogen at Scale. *Annu Rev Chem Biomol Eng* **2019**, *10* (1), 219–239. https://doi.org/10.1146/annurev-chembioeng-060718-030241.

(2) Pivovar, B.; Rustagi, N.; Satyapal, S. Hydrogen at Scale (H_2 @Scale): Key to a Clean, Economic, and Sustainable Energy System. *Electrochem Soc Interface* **2018**, *27* (1), 47–52. https://doi.org/10.1149/2.F04181if.

(3) International, I. E. A.; Agency, E. Global Hydrogen Review. **2021**.

(4) Krivina, R. A.; Ou, Y.; Xu, Q.; Twight, L. P.; Stovall, T. N.; Boettcher, S. W. Oxygen Electrocatalysis on Mixed-Metal Oxides/Oxyhydroxides: From Fundamentals to Membrane Electrolyzer Technology. *Acc Mater Res* **2021**, *2* (7), 548–558. https://doi.org/10.1021/accountsmr.1c00087.

(5) Ayers, K. Gigawatt-Scale Renewable Hydrogen via Water Splitting as a Case Study for Collaboration: The Need to Connect Fundamental and Applied Research to Accelerate Solutions. *MRS Energy & Sustainability* **2017**, *4* (June), 1–10. https://doi.org/10.1557/mre.2017.13.

(6) Ayers, K. E.; Anderson, E. B.; Capuano, C.; Carter, B.; Dalton, L.; Hanlon, G.; Manco, J.; Niedzwiecki, M. Research Advances towards Low Cost, High Efficiency PEM Electrolysis. *ECS Trans* **2010**, *33* (1), 3–15. https://doi.org/10.1149/1.3484496/XML.

(7) Allen J. Bard and Larry R. Faulkner, *Electrochemical Methods: Fundamentals and Applications*, New York: Wiley, 2001, 2nd ed.. *Russian Journal of Electrochemistry* **38**, 1364–1365 (2002). https://doi.org/10.1023/A:1021637209564

(8) Yang, J.; Jang, M. J.; Zeng, X.; Park, Y. S.; Lee, J.; Choi, S. M.; Yin, Y. Non-Precious Electrocatalysts for Oxygen Evolution Reaction in Anion Exchange Membrane Water Electrolysis: A Mini Review. *Electrochem commun* **2021**, *131*, 107118. https://doi.org/10.1016/j.elecom.2021.107118.

(9) Ehelebe, K.; Ashraf, T.; Hager, S.; Seeberger, D.; Thiele, S.; Cherevko, S. Fuel Cell Catalyst Layer Evaluation Using a Gas Diffusion Electrode Half-Cell: Oxygen Reduction Reaction on Fe-N-C in Alkaline Media. *Electrochem commun* **2020**, *116* (May), 106761. https://doi.org/10.1016/j.elecom.2020.106761.

(10) Anderson, G. C.; Pivovar, B. S.; Alia, S. M. Establishing Performance Baselines for the Oxygen Evolution Reaction in Alkaline Electrolytes. *J Electrochem Soc* **2020**, *167* (4), 044503. https://doi.org/10.1149/1945-7111/ab7090.

(11) Lindquist, G. A.; Xu, Q.; Oener, S. Z.; Boettcher, S. W. Membrane Electrolyzers for Dirty-Water Splitting. 1–13.

(12) Krivina, R. A.; Lindquist, G. A.; Yang, M. C.; Cook, A. K.; Hendon, C. H.; Motz, A. R.; Capuano, C.; Ayers, K. E.; Hutchison, J. E.; Boettcher, S. W. Three-Electrode Study of Electrochemical Ionomer Degradation Relevant to Anion-Exchange-Membrane Water Electrolyzers. *ACS Appl Mater Interfaces* **2022**. https://doi.org/10.1021/acsami.1c22472.

(13) Wang, J.; Zhao, Y.; Setzler, B. P.; Rojas-Carbonell, S.; Ben Yehuda, C.; Amel, A.; Page, M.; Wang, L.; Hu, K.; Shi, L.; Gottesfeld, S.; Xu, B.; Yan, Y. Poly(Aryl Piperidinium) Membranes and Ionomers for Hydroxide Exchange Membrane Fuel Cells. *Nat Energy* **2019**, *4* (5), 392–398. https://doi.org/10.1038/S41560-019-0372-8.

(14) Soni, R.; Miyanishi, S.; Kuroki, H.; Yamaguchi, T. Pure Water Solid Alkaline Water Electrolyzer Using Fully Aromatic and High-Molecular-Weight Poly(Fluorene- Alt-Tetrafluorophenylene)-Trimethyl Ammonium Anion Exchange Membranes and Ionomers. *ACS Appl Energy Mater* **2021**, *4* (2), 1053–1058. https://doi.org/10.1021/acsaem.0c01938.
(15) Lindquist, G. A.; Oener, S. Z.; Krivina, R.; Motz, A. R.; Keane, A.; Capuano, C.; Ayers, K. E.; Boettcher, S. W. Performance and Durability of Pure-Water-Fed Anion Exchange Membrane Electrolyzers Using Baseline Materials and Operation. *ACS Appl Mater Interfaces* **2021**, *13* (44), 51917–51924. https://doi.org/10.1021/acsami.1c06053.
(16) Huang, G.; Mandal, M.; Hassan, N. U.; Groenhout, K.; Dobbs, A.; Mustain, W. E.; Kohl, P. A. Ionomer Optimization for Water Uptake and Swelling in Anion Exchange Membrane Electrolyzer: Oxygen Evolution Electrode. *J Electrochem Soc* **2020**, *167* (16), 164514. https://doi.org/10.1149/1945-7111/abcde3.
(17) Bernt, M.; Gasteiger, H. A. Influence of Ionomer Content in IrO 2 /TiO 2 Electrodes on PEM Water Electrolyzer Performance . *J Electrochem Soc* **2016**, *163* (11), F3179–F3189. https://doi.org/10.1149/2.0231611jes.
(18) Li, D.; Motz, A. R.; Bae, C.; Fujimoto, C.; Yang, G.; Zhang, F.-Y.; Ayers, K. E.; Kim, Y. S. Durability of Anion Exchange Membrane Water Electrolyzers. *Energy Environ. Sci* **2021**, *14*, 3393. https://doi.org/10.1039/d0ee04086j.
(19) Hassan, N. U.; Zheng, Y.; Kohl, P. A.; Mustain, W. E. KOH vs Deionized Water Operation in Anion Exchange Membrane Electrolyzers. *J Electrochem Soc* **2022**, *169* (4), 044526. https://doi.org/10.1149/1945-7111/ac5f1d.
(20) Jhong, H. R. Q.; Brushett, F. R.; Kenis, P. J. A. The Effects of Catalyst Layer Deposition Methodology on Electrode Performance. *Adv Energy Mater* **2013**, *3* (5), 589–599. https://doi.org/10.1002/aenm.201200759.
(21) Li, D.; Motz, A. R.; Bae, C.; Fujimoto, C.; Yang, G.; Zhang, F. Y.; Ayers, K. E.; Kim, Y. S. Durability of Anion Exchange Membrane Water Electrolyzers. *Energy Environ Sci* **2021**, *14* (6), 3393–3419. https://doi.org/10.1039/d0ee04086j.
(22) Xu, D.; Stevens, M. B.; Cosby, M. R.; Oener, S. Z.; Smith, A. M.; Enman, L. J.; Ayers, K. E.; Capuano, C. B.; Renner, J. N.; Danilovic, N.; Li, Y.; Wang, H.; Zhang, Q.; Boettcher, S. W. Earth-Abundant Oxygen Electrocatalysts for Alkaline Anion-Exchange-Membrane Water Electrolysis: Effects of Catalyst Conductivity and Comparison with Performance in Three-Electrode Cells. *ACS Catal* **2019**, *9* (1), 7–15. https://doi.org/10.1021/acscatal.8b04001.
(23) Krivina, R. A.; Lindquist, G. A.; Beaudoin, S. R.; Stovall, T. N.; Thompson, W. L.; Twight, L. P.; Marsh, D.; Grzyb, J.; Fabrizio, K.; Hutchison, J. E.; Boettcher, S. W. Anode Catalysts in Anion-Exchange-Membrane Electrolysis without Supporting Electrolyte: Conductivity, Dynamics, and Ionomer Degradation. *Advanced Materials* **2022**, *34* (35), 1–10. https://doi.org/10.1002/adma.202203033.
(24) Glenn, J. R.; Lindquist, G. A.; Roberts, G. M.; Boettcher, S. W.; Ayers, K. E. Standard Operating Procedure for Post-Operation Component Disassembly and Observation of Benchtop Water Electrolyzer Testing. *Front Energy Res* **2022**, *10* (August), 1–10. https://doi.org/10.3389/fenrg.2022.908672.
(25) Stevens, M. B.; Enman, L. J.; Korkus, E. H.; Zaffran, J.; Trang, C. D. M.; Asbury, J.; Kast, M. G.; Toroker, M. C.; Boettcher, S. W. Ternary Ni-Co-Fe Oxyhydroxide Oxygen Evolution Catalysts: Intrinsic Activity Trends, Electrical Conductivity, and Electronic

Band Structure. *Nano Res* **2019**, *12* (9), 2288–2295. https://doi.org/10.1007/s12274-019-2391-y.
(26) Dette, C.; Hurst, M. R.; Deng, J.; Nellist, M. R.; Boettcher, S. W. Structural Evolution of Metal (Oxy)Hydroxide Nanosheets during the Oxygen Evolution Reaction. *ACS Appl Mater Interfaces* **2019**, *11* (6), 5590–5594. https://doi.org/10.1021/acsami.8b02796.
(27) McCrory, C. C. L.; Jung, S.; Peters, J. C.; Jaramillo, T. F. Benchmarking Heterogeneous Electrocatalysts for the Oxygen Evolution Reaction. *J Am Chem Soc* **2013**, *135* (45), 16977–16987. https://doi.org/10.1021/ja407115p.
(28) Louie, M. W.; Bell, A. T. An Investigation of Thin-Film Ni-Fe Oxide Catalysts for the Electrochemical Evolution of Oxygen. *J Am Chem Soc* **2013**, *135* (33), 12329–12337. https://doi.org/10.1021/ja405351s.
(29) Burke, M. S.; Enman, L. J.; Batchellor, A. S.; Zou, S.; Boettcher, S. W. Oxygen Evolution Reaction Electrocatalysis on Transition Metal Oxides and (Oxy)Hydroxides: Activity Trends and Design Principles. *Chemistry of Materials* **2015**, *27* (22), 7549–7558. https://doi.org/10.1021/acs.chemmater.5b03148.
(30) Trotochaud, L.; Young, S. L.; Ranney, J. K.; Boettcher, S. W. Nickel-Iron Oxyhydroxide Oxygen-Evolution Electrocatalysts: The Role of Intentional and Incidental Iron Incorporation. *J Am Chem Soc* **2014**, *136* (18), 6744–6753. https://doi.org/10.1021/ja502379c.
(31) Trotochaud, L.; Ranney, J. K.; Williams, K. N.; Boettcher, S. W. Solution-Cast Metal Oxide Thin Film Electrocatalysts for Oxygen Evolution. *J Am Chem Soc* **2012**, *134* (41), 17253–17261. https://doi.org/10.1021/ja307507a.
(32) Stevens, M. B.; Trang, C. D. M.; Enman, L. J.; Deng, J.; Boettcher, S. W. Reactive Fe-Sites in Ni/Fe (Oxy)Hydroxide Are Responsible for Exceptional Oxygen Electrocatalysis Activity. *J Am Chem Soc* **2017**, *139* (33), 11361–11364. https://doi.org/10.1021/jacs.7b07117.
(33) Wiegmann, T.; Pacheco, I.; Reikowski, F.; Stettner, J.; Qiu, C.; Bouvier, M.; Bertram, M.; Faisal, F.; Brummel, O.; Libuda, J.; Drnec, J.; Allongue, P.; Maroun, F.; Magnussen, O. M. Operando Identification of the Reversible Skin Layer on Co3O4as a Three-Dimensional Reaction Zone for Oxygen Evolution. *ACS Catal* **2022**, 3256–3268. https://doi.org/10.1021/acscatal.1c05169.
(34) Biesinger, M. C.; Lau, L. W. M.; Gerson, A. R.; Smart, R. S. C. The Role of the Auger Parameter in XPS Studies of Nickel Metal, Halides and Oxides. *Physical Chemistry Chemical Physics* **2012**, *14* (7), 2434–2442. https://doi.org/10.1039/c2cp22419d.
(35) Bergmann, A.; Jones, T. E.; Martinez Moreno, E.; Teschner, D.; Chernev, P.; Gliech, M.; Reier, T.; Dau, H.; Strasser, P. Unified Structural Motifs of the Catalytically Active State of Co(Oxyhydr)Oxides during the Electrochemical Oxygen Evolution Reaction. *Nat Catal* **2018**, *1* (9), 711–719. https://doi.org/10.1038/s41929-018-0141-2.
(36) Chen, J.; Selloni, A. Electronic States and Magnetic Structure at the Co 3O 4(110) Surface: A First-Principles Study. *Phys Rev B Condens Matter Mater Phys* **2012**, *85* (8), 1–9. https://doi.org/10.1103/PhysRevB.85.085306.